Revision 1

Preservation of organic matter in nontronite against iron redox cycling

Qiang Zeng [1], Hailiang Dong [1,2 *], Linduo Zhao [2], and Qiuyuan Huang [2]

[1] State Key Laboratory of Biogeology and Environmental Geology
China University of Geosciences, Beijing 100083, P. R. China

[2] Department of Geology and Environmental Earth Science
Miami University, Ohio 45056, USA

Authors to whom correspondence should be addressed
(donghg@cugb.edu.cn or donghg@miamioh.edu)

Revised for American Mineralogist

July 24, 2015

Abstract

It is generally believed that clay minerals can protect organic matter from degradation in redox active environments, but both biotic and abiotic factors can influence the redox process and thus potentially change the clay-organic association. However, the specific mechanisms involved in this process remain poorly understood. In this study, a model organic compound, 12-Aminolauric acid (ALA) was selected to intercalate into the structural interlayer of nontronite (an iron-rich smectite, NAu-2) to form an ALA-intercalated NAu-2 composite (ALA-NAu-2). *Shawanella putrefaciens* CN32 and sodium dithionite were used to reduce structural Fe(III) to Fe(II) in NAu-2 and ALA-NAu-2. The bioreduced ALA-NAu-2 was subsequently re-oxidized by air. The rates and extents of bioreduction and air re-oxidation were determined with wet chemistry methods. ALA release from ALA-NAu-2 via the redox process was monitored. Mineralogical changes after iron redox cycle were investigated with X-ray diffraction, infrared spectroscopy, and scanning and transmission electron microscopy. At the beginning stage of bioreduction, *S. putrefaciens* CN32 reductively dissolved small and poorly crystalline particles and released intercalated ALA, resulting a positive correlation between ALA release and iron reduction extent (<12%). The subsequent bioreduction (reduction extent from 12~30%) and complete air re-oxidation showed no effect on ALA release. These results suggest that released ALA was largely from small and poorly crystalline NAu-2 particles. In contrast to bioreduction, chemical reduction did not exhibit any selectivity in reducing

ALA-NAu-2 particles, and a considerable amount of reductive dissolution was responsible for a large amount of ALA release (>80%). Because bacteria are the principal agent for mediating redox process in natural environments, our results demonstrated that the structural interlayer of smectite can serve as a potential shelter to protect organic matter from oxidation.

Key words: nontronite, iron redox cycle, organic matter preservation

INTRODUCTION

The largest carbon sinks on earth are the ocean and land ecosystems, which absorb a half of the carbon dioxide emission produced by anthropogenic activities (Houghton, 1996). Organic carbon is a highly dynamic carbon repository and its turnover time has a major impact on carbon cycling. A large fraction of organic carbon is associated with minerals, especially clay minerals, largely because of their large surface area (Mayer, 1994a), diverse types of charges on surfaces and edges (Hedges and Hare, 1987), pronounced cation exchange capacity in the expandable interlayer region (Kennedy et al. 2002; Theng et al. 1986), and irregular intra/inter-granular microstructures (Bock and Mayer, 2000). Association of organic matter with clay minerals can significantly reduce its bioavailability and slow down mineralization rate (Conant et al. 2011; Jones and Edwards, 1998; Keil et al. 1994a), thus reducing the amount of CO_2 flux from the land to the atmosphere.

Abundant evidence has accumulated over the last few decades about the relationship between clay minerals and organic matters in a wide range of environments, such as seafloor sediments (Keil et al. 1994a), continental margin (Mayer, 1999; Mayer, 1994b; Ransom et al. 1998), terrestrial soils (Kaiser and Guggenberger, 2000; Mayer, 1994a), and sedimentary rocks (Kennedy et al. 2006; Kennedy et al. 2002). Several mechanisms have been proposed to explain the association between clay minerals and organic matter, such as external surface adsorption via ligand or ion exchange, cation bridging, Van der Waals forcing

(Arnarson and Keil, 2001; Bergamaschi et al. 1997; Kaiser and Guggenberger, 2000; Keil et al. 1994b; Keil and Mayer, 2014; Kleber et al. 2014; Mayer, 1994a, b; Ransom et al. 1998), and particle flocculation and aggregation(Bock and Mayer, 2000). However, the fate of organic matter in the interlayer region of clay minerals has received relatively little attention, possibly because it is difficult to accurately characterize and quantify it (Keil and Mayer, 2014). However, several studies have identified such intercalated organic matter in clay minerals, mostly through indirect evidence (Kennedy et al, 2002; Theng et al, 1986). A recent study found that the acidic interlayer sites of montmorillonite can promote thermal degradation of interlayer organics (Yuan et al. 2012). Approximately 43 times more C_{1-5} hydrocarbons were generated from the interlayer intercalated–organic matter than from organic matter alone. Thus, it is likely that the interlayer region of clay minerals is not only a potential storage space for stabilizing organic matter, but also plays an important role in organic matter maturation and fossil fuel generation. Therefore, prior to deep burial and diagenesis, these clay-organic matter associations may be subjected to biotic and abiotic redox processes.

Most clay minerals contain variable amounts of structural iron, and the oxidation state of structural iron affects their physical and chemical properties such as specific surface area, basal spacing and degree of swelling, layer charge, cation exchange capacity (Stucki, 2011; Stucki and Kostka, 2006), and their association with organic matter (Zhang et al. 2007; Zhang et al. 2014). The cycling of iron valence state can be achieved either biologically or chemically. To date, numerous studies have shown the

important role of microbes in the iron redox cycle (Weber et al. 2006; Melton et al., 2014). Recently, a wide variety of microorganisms isolated from diverse environments have been used to either reduce or oxidize structural iron in clay minerals (Dong et al. 2009; Dong 2012; Pentráková et al. 2013; Stucki and Kostka, 2006; Stucki 2011; Zhao et al., 2015).

During the last decades, many studies have revealed that the biogeochemical cycles of iron and organic carbon are strongly linked in various environments (Jonhson et al. 1997; Kaiser and Guggenberger, 2000; Lalonde et al. 2012). These authors found that reactive iron phases (such as iron oxides) can promote organic carbon preservation through co-precipitation and/or direct chelation. Reductive dissolution of such iron phases can release the associated organic carbon. Moreover, several model experiments have studied the relationship between iron reduction and organic carbon release from clay minerals. For example, Zhang et al. (2007) found that organic compounds cysteine and toluene can be intercalated into the nontronite interlayers, and microbial dissolution of its structural Fe(III) can partially release these compounds, but the extent of release depends on the type of organic matter in the interlayer. Most recently, Zhang et al. (2014) showed that reductive dissolution mediated by a methanogen could partially release a model organic compound. However, it remains unclear if a similar mechanism operates by other bacteria such as dissimilatory iron-reducing bacteria. The physiological difference between methanogen and iron-reducing bacteria may be important to the release and the fate of ALA. A systematic comparison of the effects of biological vs. chemical reduction on

clay structural alterations and organic matter release mechanism is also lacking. The stability of clay-associated organic compound against a complete iron redox cycle (e.g. reduction followed by oxidation) is currently unknown. Furthermore, the impact of organic matter on clay structural and mineral transformation is poorly understood.

To achieve these goals, a model organic compound, 12-Aminolauric acid (ALA) was intercalated into the interlayer of an iron-rich smectite, nontronite (NAu-2), to synthesize an organoclay ALA-NAu-2. The choice of nontronite was to facilitate a mechanistic understanding of Fe redox process and its impact on organic compound stability within the mineral. A well-studied dissimilatory iron reducing bacterium (DIRB) *Shawanella putrefaciens* CN32 and sodium dithionite were used as a biological and a chemical reducing agent, respectively. After the intercalation of ALA into the nontronite interlayer, the resulting organoclay was subjected to bioreduction by *S. putrefaciens* CN32 and air re-oxidation to assess the effects of iron redox cycling on ALA preservation within the nontronite structure. Various geochemical and mineralogical methods were used to examine the reaction progress, ALA release, and mineralogical changes. Our results demonstrated that the release pattern of ALA from the nontronite interlayer was dependent on the Fe(III) reduction mechanism. Reductive dissolution of small and poorly crystalline particles as triggered by bioreduction resulted in ALA release at the beginning, but subsequent reduction of structural Fe(III) from larger and more crystalline particles did not further release ALA. In contrast, chemical reduction largely destroyed the nontronite structure and resulted in a nearly complete release of ALA.

MATERIALS AND METHODS

Clay mineral preparation

Nontronite (NAu-2) was purchased from the Source Clays Repository of the Clay Minerals Society (West Lafayette, IN). The formula of NAu-2 was $(K_{0.01}Na_{0.30}Ca_{0.15})(Al_{0.55}Fe^{3+}_{3.27}Fe^{2+}_{0.06}Mg_{0.12})(Si_{7.57}Al_{0.15}Fe^{3+}_{0.28})O_{20}(OH)_4$ (Keeling et al. 2000). The bulk sample was manually ground and soaked in 0.5 N NaCl solution for 24 hrs with constant stirring. A specific size fraction (0.02-0.5 μm) was collected by repeated centrifugation and washing with doubly distilled water. The cation exchange capacity of this fraction was 697.1 (±73.4) meq/kg, as previously determined using the NH_4^+ exchange method (Jaisi et al. 2008b). The removal of excess chlorine anion was confirmed with the $AgNO_3$ test. Our XRD analysis confirmed our previous studies (Jaisi et al. 2005; Yang et al. 2012; Zhao et al. 2015) in showing that this size fraction consisted of pure nontronite without any iron oxides.

Synthesis of organo-clay composite

12-Aminolauric acid (ALA) $[NH_2(CH_2)_{11}COOH]$ was chosen as a model organic compound. ALA is a non-conductive molecule and very stable in neutral environment. The isoelectric point of ALA is about 2. ALA is not an effective carbon source for *Shewanella* species. In this study, ALA was chosen based on two reasons. First, it contains both carboxyl groups and alkyl chains with moderate carbon numbers, which are typical of natural organics associated with clay minerals (Wattel-Koekkoek et al. 2011). Second, the aminopropyl group ($-NH_2$) of ALA is readily transformed to

178 protonated amino group ($-NH_3^+$) in acidic solution, and therefore, it can be
179 intercalated into the NAu-2 interlayer via cation exchange.

180 Before the ALA intercalation experiment, five grams of the prepared NAu-2 size
181 fraction were placed in a clean beaker and stirred with 500 ml deionized water
182 overnight to allow complete dispersion of the NAu-2 slurry. An ALA solution was
183 made with a concentration approximately twice the cation exchange capacity (CEC)
184 of the prepared NAu-2. Before its addition to the NAu-2 solution, ALA was
185 protonated by mixing with HCl solution (0.07 N; pH=1.14) at 80℃. The protonation
186 reaction was considered complete when the ALA solution became clear. The NAu-2
187 and ALA solutions were then mixed and stirred vigorously for 30 minutes in an 80℃
188 water bath (pH=4.5). The synthesized organo-NAu-2 complex (termed as
189 ALA-NAu-2 hereafter) was collected by repeated centrifugation and washing with
190 80℃ double distilled water (five times) to remove any free and weakly sorbed ALA.
191

192 **Biological reduction and air re-oxidation experiments**

193 *Shawanella putrefaciens* strain CN32 was isolated from an anaerobic subsurface
194 core sample (250 m beneath the surface) obtained from the Morrison Formation in
195 northwestern New Mexico (Fredrickson et al, 1998). CN32 cells were routinely
196 cultured in tryptic soy broth (TSB) aerobically from the stock culture, which was kept
197 in 40% glycerol at -80°C. The cells of the exponential growth phase were harvested,
198 washed with sterilized bicarbonate buffer (2.5 g/L reagent grade $NaHCO_3$) three times
199 to completely remove any residual TSB, and re-suspended in sterilized bicarbonate

buffer for inoculation.

Both NAu-2 and ALA-NAu-2 were made into slurries (final conc. 5 g/L) with bicarbonate buffer (2.5 g/L reagent grade $NaHCO_3$). Bioreduction experiments were conducted in serum bottles sealed with rubber stoppers and aluminum caps after the clay slurries were purged with N_2:CO_2 (80:20) (clay suspension volume 80 ml, total volume of the bottles 120 ml). After autoclaving, filter-sterilized lactate was injected to serve as the sole electron donor with a final concentration 10 mM. In selected groups, sterilized anthraquinone-2,6-disulfonate (AQDS) was added as an electron shuttling compound to facilitate the electron transfer (final conc. 0.1 mM). Finally bicarbonate-washed CN32 cells were injected into the serum bottles to achieve a cell concentration of 10^8 cells/ml (acridine orange direct count, AODC). Both the NAu-2 and ALA-NAu-2 experiments consisted of three groups: a). Abiotic control group containing lactate and AQDS but without cells; b). Experimental group 1 containing lactate and CN32 cells without AQDS; c). Experimental group 2 containing lactate and CN32 cells but with AQDS. All treatments were performed in duplicates. The serum bottles were incubated at 37℃ with constant shaking to prevent solid precipitation.

Although the microbial Fe(III) reduction activity ceased in 10 days, the subsequent re-oxidation experiment was not commenced until 30 days. In an anaerobic glove box filled with 95% N_2 and 5% H_2 (Coy Laboratory Products, Grass Lake, MI, USA), the bioreduced clay suspensions in the serum bottles were pasteurized in a water bath (80^oC, 3 times each at 30 mins) followed by transfer to

27-mL Balch tubes (final clay suspension volume 15 ml) without any washing in order to protect the integrity of the clay particles. To avoid evaporation during the re-oxidation process, the Balch tubes were sealed with rubber stoppers but with two needles inserted into it. One needle was used as an air inlet and the other as a vent. Re-oxidation of the reduced clay fractions was started by constantly bubbling air through the needle and continued for 10 days.

Chemical reduction and air re-oxidation experiments

In order to compare the reduction kinetics and ALA release patterns between biotic and abiotic reduction, ALA-NAu-2 was also chemically reduced using sodium dithionite (Stucki et al. 1996). To achieve different Fe(III) reduction extents, six different sodium dithionite/mineral ratios (from 0.5:1 to 8:1) were used in the reduction experiments. The reduction procedure was the same as the bioreduction experiment except that sodium dithionite replaced CN32 cells without lactate and AQDS.

Analytical methods

Chemical analyses. To monitor the progress of Fe(III) reduction and Fe(II) oxidation in NAu-2 and ALA-NAu-2, the total Fe(II) concentration was measured with the 1,10-phenanthroline method (Amonette and Templeton, 1998). At selected time points, 0.2 ml homogenized clay slurry was sampled with an anoxic and sterile syringe followed by the Fe(II) measurement. To detect any reductive dissolution of NAu-2

and ALA-NAu-2 after the Fe redox cycle, those samples from the beginning and the end of reduction and re-oxidation experiments were also measured for aqueous concentrations of Fe, Al, and Si. Approximately 5 ml of homogenized clay slurries were sampled and centrifuged inside an anaerobic glove box. Aqueous Fe, Al, and Si concentrations in the supernatants were measured with inductively coupled plasma optical emission spectrophotometry (ICP–OES) (Agilent Technologies 700 Series).

X-ray diffraction (XRD). XRD was performed to detect mineralogical changes of both NAu-2 and ALA-NAu-2 after reduction and re-oxidation. Approximately 0.5 ml clay slurries were sampled and smeared onto petrographic glass slides and dried overnight in an anaerobic glove box. Samples were also treated with ethylene glycol (EG) in order to distinguish between smectite and illite. XRD patterns were obtained with a Rigaku Smart lab X-ray powder diffractometer using CuKα radiation, rotating-anode generator, and a power of 8500 W (200 kV, 45 mA). The samples were scanned from 2 to 15° 2-theta stepping at 0.02 with a count time of 1s per step.

For modeling of the diffraction peaks, a Gauss peak-fitting method was applied to selected XRD patterns with the Origin 8.5 program. The fitting region was between 3° to 12° to ensure that the whole peak area was covered. A multi peak fitting method was applied to automatically detect and deconvolute overlapping peaks.

Fourier transform infrared spectroscopy (FTIR). In order to confirm ALA intercalation into the interlayer of NAu-2 and to detect any change of chemical

bonding of ALA and ALA-NAu-2 after the iron redox cycle, unreduced, reduced, and re-oxidized NAu-2 and ALA-NAu-2 were prepared for FTIR analysis in the mid-infrared region. In an anaerobic glove box, 0.4 ml clay slurry was sampled from the sample serum bottle followed by centrifugation to acquire a pellet. After washing with anoxic distilled water (3 times), the clay pellet was allowed to dry inside an anaerobic glove box for over 24 hrs. Subsequently, two milligrams of the dried clay pellet were manually mixed with 200 mg KBr and pressed into discs. The samples were immediately analyzed in the diffuse reflectance mode using a Perkin-Elmer Frontier Infrared Spectrometer. Fifty scans over the range 400–4000 cm^{-1} with a spectral resolution of 4 cm^{-1} were accumulated for each spectrum. The Origin 8.5 program was applied to calculate the specific peak areas.

Total organic carbon (TOC) measurement. Time-course TOC measurement was made to monitor its release due to Fe reduction and re-oxidation. Approximately six milliliters of homogenized clay slurry were sampled inside a glove box and washed with anoxic DI water (3 times). After drying, TOC content was measured using an Analytik-jena multi series analyzer with a furnace temperature of 1000°C.

Scanning electron microscopy (SEM). To further detect mineralogical changes of NAu-2 and ALA-NAu-2 after the iron redox cycle, these clay minerals were observed under SEM. Clay suspensions were mounted on glass cover slips and fixed with a mixture of 2% paraformaldehyde and 2.5% glutaraldehyde. These sample-containing

cover slips were then sequentially dehydrated in varying proportions of ethanol followed by critical point drying with a Quorum K850 Critical Point Dryer (CPD) (Dong et al., 2003). After drying, the sample-coated cover slips were mounted on SEM stubs and Pt-coated with Quorum SC7620 Sputter Coater for SEM observations. A Zeiss Supra 55 SAPPHIRE SEM with Genesis 2000 X-ray energy dispersive spectroscopy (SEM/EDS) was employed for morphological observation and chemical analysis. The SEM was operated at an accelerating voltage of 8-15 kV. A working distance (15 mm) and low beam current (30-40 μA) were used to achieve the best image resolution. A higher beam current (50-70 μA) was used for qualitative EDS.

Transmission electron microscopy (TEM). To further confirm ALA intercalation into the interlayer of NAu-2 and to detect any mineralogical change after the Fe redox cycle, TEM observations were made. Clay slurries were diluted by a factor of 50, and pipetted onto 300 mesh copper grids with carbon-coated nitrocellulose membrane. The grids were allowed to dry overnight inside an anaerobic glove box. TEM imaging and analysis were performed with a JEOL JEM-2100 LaB6 TEM/STEM with a 200 keV accelerating voltage. The bright-field imaging mode (TEM BF) was used to study the morphology of clay particles. TEM images were recorded using a Gatan Orius SC200D camera attached on a Gatan 863 Tridiem GIF Post-Column Energy Filter EELS/EFTEM (Gatan Image Filter).

RESULTS

Characterization of ALA-NAu-2

Physical and chemical characteristics. In comparison with NAu-2, ALA-NAu-2 became fluffy in texture and light green in color. When NAu-2 and ALA-NAu-2 were made into slurries and stirred for 24 hrs, the former turned into a homogeneous colloidal suspension (Fig. 1A, left), whereas the latter settled down in a few minutes (Fig. 1A, right). This physical difference between NAu-2 and ALA-NAu-2 suggested an association of ALA with NAu-2. SEM images did not exhibit any obvious morphological difference between NAu-2 and ALA-NAu-2 (Fig. 1 B & C). Particles in both NAu-2 and ALA-NAu-2 showed a flaky texture with a low Al/Si ratio (Fig. 1 D & E). The carbon content was higher in ALA-NAu-2 than in NAu-2, again suggesting an association of ALA with NAu-2. The total iron content decreased from 23.9% in NAu-2 to 19.9% in ALA-NAu-2, of which 99% was Fe(III). In contrast, total organic carbon (TOC) content increased from 0.97% in NAu-2 to 6% in ALA-NAu-2.

XRD and FTIR. XRD and FTIR results further indicated that ALA was intercalated into the interlayer region of NAu-2. For the air-dried samples, the d(001) spacing increased from 12.33 Å for NAu-2 to 17.10 Å for ALA-NAu-2 (Fig. 2 A & B). In addition, the d(001) peak was broader in ALA-NAu-2 than the same peak in NAu-2, suggesting that the intercalation of ALA into the interlayer region of NAu-2 may have decreased crystallinity and/or particle size of NAu-2, consistent with a previous observation (Liu et al. 2011).

To further confirm that the d(001) layer expansion was due to the intercalation of ALA, FTIR spectroscopy was performed on ALA-NAu-2 and a mechanical mixture of ALA and NAu-2 (in the same ratio as that used for ALA-NAu-2 synthesis, termed as ALA+NAu-2). Almost all the characteristic absorption bands of ALA were present in ALA+NAu-2, but only a subset of ALA bands were visible in ALA-NAu-2 with some minor shifts in wave number (Fig. 3), suggesting that the ALA and NAu-2 association in ALA-NAu-2 was via interlayer intercalation, not due to physical mixing.

Specifically, the broad H–OH stretching band for the molecular water in the interlayer region of NAu-2 became weaker in the ALA-NAu-2 (Fig. 3A, a & d centered at 3426 cm^{-1}), suggesting a partial replacement of adsorbed interlayer water by intercalated ALA (Katti et al. 2006). A sharp N-H stretching band at 3236 cm^{-1} that was clearly observed in pure ALA became invisible in ALA-NAu-2, possibly because this small band may be buried under a broad H-OH hydrogen bonded water (3500-3200 cm^{-1}) (Fig. 3A, b &d) (Neumann et al. 2011; Sikdar et al. 2008).

Two sharp absorption bands at 2923 and 2851 were observed for pure ALA and they were assigned to C-H asymmetric and symmetric stretching, respectively (Fig. 3B, b) (Katti et al. 2006; Sikdar et al. 2008). In ALA+NAu-2, these two bands stayed at the same positions (Fig. 3B, c). However, in ALA-NAu-2, these absorption bands became weaker and broader, and shifted slightly to higher wave numbers (from 2923 to 2930, 2851 to 2855, respectively) (Fig. 3B, d). It has been reported that the orientation of intercalated ALA in smectite should be flat and parallel to the smectite

layer (Katti et al. 2008; Sikdar et al. 2006a). Thus, the interaction of oriented ALA in the interlayer space of NAu-2 with the tetrahedral layers above and below might have caused these wave number shifts (Katti et al. 2006; Sikdar et al. 2006a).

In the 1700-1550 cm^{-1} region, the broad absorption peak at 1633 cm^{-1} was assigned to the O-H deformation in NAu-2 (Fig. 3D, a) (Katti et al. 2006; Sikdar et al. 2008). A sharp absorption band at 1637 cm^{-1} was observed for pure ALA that could be assigned to a combination of O-H deformation and N-H bending (Fig. 3D, b) (Katti et al. 2006). In ALA + NAu-2, these two bands were superimposed to produce a broad peak centered at 1642 (Fig. 3D, c). In ALA-NAu-2, this composite band became even broader and its center shifted to 1627 cm^{-1} (Fig. 3D, d). This shift can be attributed to the electrostatic interaction of the functional groups of ALA with the surface oxygen of the Si-O_4 tetrahedra present above and below the NAu-2 interlayer. The broad peak shape may be a result of the replacement of interlayer water in NAu-2 by ALA, further confirming the intercalation of ALA (Katti et al. 2006; Sikdar et al. 2006a; Sikdar et al. 2008).

In pure ALA solid, the carboxyl functional group should remain in dissociated form (R-COO^-) and therefore gave rise to the asymmetric and symmetric stretching bands at 1514 and 1396 cm^{-1}, respectively (Fig. 3E, b) (Katti et al. 2006; Sikdar et al. 2008). During the intercalation process, ALA was protonated in aqueous solution, and the COO^- group was converted to the COOH group, which appeared to cause the emergence of a carbonyl absorption band (C=O) (e.g. 1711 cm^{-1}) (Katti et al. 2006). Thus, the protonation of COO^- to COOH in ALA-NAu-2 resulted in disappearance of

1514 and 1396 cm^{-1} (Fig. 3E, d) and emergence of an absorption band at 1711 cm^{-1} (Fig. 3C, d).

Microbial reduction of structural Fe(III) and air re-oxidation of biogenic Fe(II) in NAu-2 and ALA-NAu-2

Reduction rate and extent. Within the experimental time frame (32 days), no reduction was observed in the abiotic control groups (Fig. 4). *S. putrefaciens* CN32 cells were able to reduce structural Fe(III) in both NAu-2 and ALA-NAu-2, but there were differences in the rate and extent of bioreduction. In the absence of AQDS, the bioreduction was complete within 32 days, with the final reduction extents of 16.8% and 15.1%, and the initial rates of 2.11×10^{-4} mM/h and 0.96×10^{-4} mM/h, for NAu-2 (Fig. 4A) and ALA-NAu-2 (Fig. 4B), respectively. A "stagnant phase" was observed in the ALA-NAu-2 group (day 5 to 12), when bioreduction apparently stopped (Fig. 4B). This "stagnant phase" was also observed in bioreduction of ALA-NAu-2 by methanogens (Zhang et al. 2014).

The presence of AQDS significantly increased both the rate and extent of bioreduction. Both NAu-2 and ALA-NAu-2 reached a similar extent of reduction by the end of 32 days (25.0% and 26.0%, respectively), but with different rates. Within the first 36 hrs, the average reduction rate was 0.081 mM/h for NAu-2, but only 0.043 mM/h for ALA-NAu-2. The highest rate during this time period (from 12 to 24 hrs) was 0.145 mM/h for NAu-2 but only 0.068 mM/h for ALA-NAu-2. These rates were almost 3 orders of magnitudes higher than those in the absence of AQDS. A "stagnant

phase" was also observed for ALA-NAu-2 around 4-5 days (Fig. 4B).

Bioreduced NAu-2 and ALA-NAu-2 exhibited a similar re-oxidation behavior. The majority of the biogenic Fe(II) (about 60%) was rapidly re-oxidized within the first 4 hrs (Fig. 5), which was consistent with a previous study (Yang et al. 2012). The fastest oxidation occurred within the first 2 hrs with rates of 1.57 mM/h and 1.19 mM/h for NAu-2 and ALA-NAu-2, respectively. The re-oxidation experiments ceased by the end of 12 hrs, but they were allowed to continue until 240 hrs to ensure complete re-oxidation. The final Fe(II)/Fe(III) ratio in ALA-NAu-2 was slightly higher than that in NAu-2 (4.7% and 3.3%, respectively).

ALA release. During the redox cycle, TOC content in the abiotic control groups of both NAu-2 and ALA-NAu-2 remained the same throughout the complete reduction (0-32 days) and oxidation (32-40 days) cycle, 6% for ALA-NAu-2 and 0.97% for NAu-2 (Fig. 6A). This constant TOC content suggested that the intercalated ALA in the interlayer of NAu-2 remained stable throughout the redox cycle. A small amount of TOC in original NAu-2 has been reported previously (Jaisi et al. 2005) and its stability over the redox cycle suggested that it was not used by any microbial activity. Bioreduction of structural Fe(III) in ALA-NAu-2 released a small amount of ALA in the first 2 days (TOC decrease from 6% to 5%), however no further release was detected afterwards (Fig. 6A). This TOC release pattern did not correspond to the bioreduction pattern (Fig. 4). For example, for the experimental group with AQDS, TOC content did not decrease any further after 2 days, even when microbial reduction

of Fe(III) was still rapid (compare Figs. 4B & Fig. 6A). The experimental group without AQDS followed the same pattern. At the end of the bioreduction, the final TOC content in ALA-NAu-2 was essentially the same regardless of the presence or absence of AQDS.

Subsequent air re-oxidation of Fe(II) in ALA-NAu-2 did not further release any ALA, as evidenced by a constant TOC content throughout the experimental duration for both abiotic control and experimental groups (dashed lines in Fig. 6A). Thus, a positive correlation (r^2=0.87) between TOC and ferrous iron content was only found when the bioreduction extent was low (<12%, Fig. 7). This correlation broke down when the extent of reduction was higher than 12%.

Aqueous cation concentrations. Aqueous concentrations of Al, Fe, and Si increased from the abiotic control to the bioreduced to the re-oxidized samples (Table 1), suggesting that a small amount of reductive and oxidative dissolution occurred as a result of iron redox cycle.

Structural changes detected by FTIR. Upon the reduction-oxidation cycle of Fe in ALA-NAu-2, the characteristic absorption bands of ALA did not shift in wave number, but increased in peak area. Specifically, the C-H asymmetric and symmetric stretching bands at ~2930 and ~2855 cm^{-1} (Fig. 3B, f & g), the C=O stretching band at ~1711 cm^{-1} (Fig. 3C, f & g), the N-H bending band at ~1627 cm^{-1} (Fig. 3D, f & g) and the CO–H bending band at ~1470 cm^{-1}(Fig. 3E, f & g) all stayed at the same positions but

442 became sharper after the redox cycle. The peak areas of these characteristic bands
443 increased after the bioreduction and air re-oxidation cycle (Table 2). In addition, the
444 N-H stretching band at 3287 cm^{-1}, which was barely visible in ALA-NAu-2 (Fig. 3A,
445 d), became distinct after the redox cycle (Fig. 3A, f & g).

446 Furthermore, the $R\text{-}COO^-$ asymmetric and symmetric stretching bands at 1514
447 and 1396 cm^{-1} became slightly more prominent in the redox-cycled samples relative
448 to the unreduced ALA-NAu-2 (Fig. 3E, d, f & g), suggesting that a small amount of
449 released ALA might have re-adsorbed onto NAu-2 particle surfaces.

450

451 **Mineralogical changes detected by XRD results.** Both air-dried and
452 ethylene-glycolated samples were examined with XRD to detect mineralogical
453 changes after bioreduction of Fe(III) and air re-oxidation of Fe(II) in NAu-2 and
454 ALA-NAu-2. Because ethylene glycol would expand the interlayer of all samples
455 (Both ALA-NAu-2 and NAu-2) to the same spacing, air dried samples were used for
456 interpreting the intercalation effect of ALA. To promote possible mineralogical
457 changes, the bioreduced NAu-2 and ALA-NAu-2 samples were incubated under the
458 same condition for additional 60 days after cessation of bioreduction. The air
459 re-oxidized samples were analyzed as soon as the re-oxidation experiments were
460 complete (i.e. after 10 days).

461 For the air-dried samples, the (001) peak remained at the same position (~17 Å,
462 $2\theta=5.20^o$) but became sharper after bioreduction of Fe(III) in ALA-NAu-2 (Fig. 2C &
463 D), suggesting little release of ALA from the NAu-2 interlayer. In addition to this

main peak, a small shoulder appeared at around 12.9 Å ($2\theta=6.88^{o}$) for the bioreduced ALA-NAu-2 sample, which was similar to the d(001) spacing of NAu-2 (Fig. 2A). This newly emerged shoulder was slightly more intense in the AQDS-treated sample than in the one without AQDS. A deconvolution of this broad "double peak" in the XRD pattern for the bioreduced ALA-NAu-2 sample (with AQDS) quantified an ALA-NAu-2/NAu-2 weight ratio of 4.29:1 (Fig. 8). This ratio suggested that 18.6% of the ALA-NAu-2 converted back to regular NAu-2 after a bioreduction-triggered loss of ALA from the interlayer of NAu-2. This amount was similar to a total of 20% ALA release from NAu-2, as determined from TOC analysis (Fig. 6A).

The small shoulder at 12.9 Å disappeared after air re-oxidation of ALA-NAu-2 with or without AQDS (Fig. 2E), and the (001) peak at 17 Å became even sharper after air re-oxidation. After the ethylene glycol treatment of ALA-NAu-2, the small shoulder disappeared and the (001) peak at 17 Å became even sharper (Appendix 1)

Mineralogical changes as evidenced by SEM and TEM observations. Bioreduction of structural Fe(III) in NAu-2 apparently broke NAu-2 into particles to form a net-like morphology with a lower amount of Fe relative to unreduced NAu-2 (Fig. 9A). Similarly, after bioreduction of structural Fe(III) in ALA-NAu-2, many dissolution pits appeared on some plate-shaped particles, forming a net-like morphology (Fig. 9B). Some particles were broken to form a lamella or even a filament-like texture. SEM/EDS analyses revealed that the platy particles contained higher amounts of iron and carbon (point b2 on Fig. 9B) than the ones with a net or

lamella-like morphology (point b1 on Fig. 9B).

Some particles in bioreduced ALA-NAu-2 exhibited a smooth surface and plate-like morphology, and EDS analysis identified them as albite (point c2 on Fig. 9C). The albite appeared to be connected to some residual iron-deficient nontronite flakes (point c1 on Fig. 9C). However, XRD did not detect any albite, possibly due to a low amount. Silica aggregates also appeared in bioreduced NAu-2 (data not shown) and ALA-NAu-2 (Fig. 9D).

In the air re-oxidized ALA-NAu-2, lamella- and filament-shaped particles that were observed in bioreduced ALA-NAu-2 disappeared. Those net-shaped flakes which were ubiquitous in bioreduced samples (Fig. 9B) were not common any more. Residual plate-shaped particles appeared to form large aggregates after air re-oxidation (Fig. 9E). The chemical composition of these aggregates (point e1) was similar to that of unreduced ALA-NAu-2 (data not shown). In addition, a few carbon-rich particles occurred within clay aggregates (Fig. 9F).

Elemental mapping of carbon in a typical plate-like bioreduced NAu-2 particle showed an uneven carbon distribution. Relative to a uniform distribution of carbon in the abiotic control group (Fig. 10A), local depletion and enrichment of carbon was apparent for bioreduced ALA-NAu-2 (Fig. 10B). Similar depletion and enrichment of carbon was also observed for air-reoxidized sample. This heterogeneous distribution of carbon suggests that carbon was re-distributed as a result of bioreduction and air re-oxidation.

TEM data provided additional evidence for mineralogical changes. In unreduced

NAu-2, the dominated d(001) spacing was 1.1-1.2 nm (Fig. 11A). After ALA intercalation into the interlayer NAu-2, the d(001) spacing increased to 1.5 nm (Fig.11B). However, this spacing was smaller than 17.1 Å as observed in XRD pattern (Fig. 2B), likely due to nontronite layer collapse inside the high vacuum of TEM. In bioreduced ALA-NAu-2, two kinds of d(001) spacings, 1.5 nm and 1.1 nm (Fig.11C), were commonly observed. These two types of spacings corresponded to the "double peaks" in the XRD profile, e.g., 17.10 and 12.33 Å (Fig. 2C & D) but with smaller values due to layer collapse. The carbon content in the 1.5 nm fringes was much higher than that in the 1.1 nm fringes (Fig.11 C), suggesting that the 1.1 nm fringes were residual NAu-2 layers after ALA loss.

Chemical reduction of structural Fe(III) in NAu-2 and ALA-NAu-2

Reduction rate and extent.

Different reduction extents (~28% to ~80%) were achieved by using different sodium dithionite to NAu-2 ratios. In contrast to bioreduction, chemical reduction was rapid and the maximum extent of reduction was reached within 2 hrs with a similar extent and rate for NAu-2 and ALA-NAu-2 (Appendix 2).

ALA release. In comparison to the bioreduced ALA-NAu-2, a different TOC release pattern was observed for chemically reduced sample. A reduction extent of 28.6% (similar to the final bioreduction extent) triggered a significant amount of TOC release (Fig. 6B). The measured amount of ALA release was not directly correlated with the

reduction extent.

Aqueous concentrations. In contrast to bioreduction, aqueous concentrations of Al, Fe, and Si in chemically reduced ALA-NAu-2 suspensions were almost two orders of magnitude higher than those for the bioreduced samples (Table 1). These concentrations increased with reduction extent.

Structural changes detected by FTIR. Unlike bioreduced ALA-NAu-2 where characteristic absorption bands did not show any significant changes in wave number, chemical reduction of ALA-NAu-2 led to significant changes in both band position and intensity. Regardless of the reduction extent, chemical reduction of Fe(III) in ALA-NAu-2 shifted the C-H asymmetric and symmetric stretching bands back to their original positions as in pure ALA (e.g. from 2930 to 2923 cm^{-1}, 2855 to 2851 cm^{-1}) with greatly decreased band intensities (Fig. 3B, i; Table. 2; data not shown for higher extents). Similar observation was made for the N-H bending band, where the peak shifted from 1633 to 1642 cm^{-1} with a decreased intensity (Fig. 3D, i; Table. 2). In addition, the C=O stretching band at 1711 cm^{-1} that was characteristic of intercalated ALA-NAu-2 disappeared after chemical reduction (Fig. 3C, i; Table. 2), again regardless of the reduction extent. The absorption peak at 1470 cm^{-1} (CO–H bending) became nearly invisible (Fig. 3E, i; Table. 2). The asymmetric and symmetric stretching bands of $R\text{-}COO^-$ at 1514 and 1396 cm^{-1} became hardly visible, suggesting that the released ALA might not be able to re-adsorb on NAu-2 particle

552 surfaces in such a short amount of time. As expected, chemically reduced NAu-2
553 exhibited similar patterns as in unreduced NAu-2 (Fig. 3A-E, h).
554
555 **Mineralogical changes detected by XRD results.** In contrast to bioreduction,
556 chemical reduction of structural Fe(III) in ALA-NAu-2 resulted in a decrease in both
557 the intensity and the spacing of the d(001) peak from 17 Å to 12.6 Å (Fig. 2F & G).
558 The 12.6 Å spacing was the nearly the same as that for the unreduced NAu-2 (Fig.
559 2A). These data are consistent with a nearly complete loss of ALA from NAu-2 upon
560 chemical reduction.
561
562 **Mineralogical changes detected by SEM observations.** Consistent with the TOC,
563 XRD, and FTIR results, SEM images for chemically reduced ALA-NAu-2 were
564 drastically different from those for the bioreduced ALA-NAu-2. Particles with rose-
565 and net-like morphologies were more common in chemically reduced samples, even
566 at the same reduction extent as in bioreduction (e.g. 28.6%, Fig. 9G). In samples with
567 a high reduction extent (>80%), dissolution pits were ubiquitous (Fig. 9H) and
568 partially dissolved particles tended to aggregate to form large networks. The contents
569 of iron and carbon decreased with increased reduction extents (Point g1 and h1 on Fig.
570 9G and 9H, respectively).
571
572
573 **DISCUSSION**

574 **Contrasting effects of interlayer ALA on biological and chemical reduction of**
575 **structural iron in nontronite**

576 A previous study systematically investigated the interaction mechanism between
577 ALA and a Na-montmorillonite at the molecular level (Katti et al. 2006) and
578 concluded that ALA entry into the montmorillonite interlayer expanded the interlayer
579 spacing. The orientation of ALA in the interlayer was parallel to the layers. Both the
580 functional groups and the backbone chain of ALA exhibited a strong interaction with
581 adjacent tetrahedral sheets above and below the intercalated interlayer, and thus
582 significantly promoted particle aggregation. Our FTIR and XRD data are consistent
583 with this study, showing that ALA intercalation into the interlayer of NAu-2
584 significantly expanded the d(001) spacing. By substituting the interlayer Na^+ and
585 molecular water, the intercalated ALA could have reduced the hydrophilicity of the
586 NAu-2, and thus promoted particle aggregation (Fig. 1) (Sikdar et al. 2006a; 2006b;
587 2008).

588 This structural configuration of ALA in the interlayer of NAu-2 would have
589 important implications for the electron transfer process. Previous studies suggested
590 that electron transfer to structural Fe(III) in clay minerals can occur both parallel and
591 perpendicular to basal planes (Dong et al. 2009; Neumann et al. 2013). Under this
592 scenario, any mechanism that alters the interlayer region would affect the electron
593 transfer pathway. For example, electron shuttling compounds such as AQDS can
594 facilitate the electron transfer process because it can possibly enter the interlayer
595 region (Bishop et al. 2011; Zhang et al. 2013). According to the same logic, the

substitution of Na^{+} and Ca^{2+} cations by ALA in the interlayer is expected to hinder the electron transfer pathway because ALA is larger than these cations. In addition, the hydrophobic and aggregated nature of ALA-intercalated NAu-2 (Fig. 1) would be unfavorable for electron transfer as well. Furthermore, the released ALA from the NAu-2 interlayer at the beginning of bioreduction could further hinder electron transfer via adsorption onto NAu-2 particle surfaces. Likewise, released ALA molecule may coat cell surfaces, which can inhibit microbial activity as well (Choi et al. 2008). These interactions work together to create an unfavorable environment for electron transfer, even with the help of hydrophilic electron shuttling compounds such as AQDS, because these compounds may not be able to enter the already congested interlayer region and/or remove ALA from NAu-2 and cell surfaces. However, the expansion of the interlayer spacing of NAu-2 by intercalated ALA should facilitate electron transfer and thus would increase the reduction rate and extent. Our data suggest that the inhibitory effect of the intercalated ALA was more important than the facilitation effect at the beginning of the bioreduction experiments and may have been responsible for the lower initial reduction rate of ALA-NAu-2 relative to NAu-2. However, the facilitation effect may become important over longer incubation time and eventually the inhibitory and facilitation effects may have canceled out with each other, resulting in no difference in the ultimate reduction extent between ALA and ALA-NAu-2 (Fig. 4).

Our current results were significantly different from our early data by Zhang et al. (2014). During a study of Fe(III) bioreduction by a methanogen *Methanosarcina*

618 *mazei* , Zhang et al. (2014) showed that ALA decreased both the rate and extent of
619 Fe(III) bioreduction, apparently because ALA blocked the electron transfer pathway,
620 even in the presence of AQDS. However, our results here did not show any inhibition
621 effect of ALA, even in the absence of AQDS. These results collectively demonstrate
622 that electron transfer pathway is dependent on both the mineral and the microbe
623 involved. Clearly, DIRB and methanogen may produce different electron transfer
624 proteins, cell appendages, and shuttling compounds, which would all contribute to
625 their difference in their Fe(III) reduction mechanisms. For example, *M. mazei* can
626 produce methanophenazine, which is a hydrophobic redox-active cofactor (Abken et
627 al. 1998), but *Shewanella* can produce menaquinone-related shuttles (Newman and
628 Kolter, 2000). These different electron shuttling compounds are expected to play
629 different roles in the electron transfer process. Future work is necessary to further
630 understand these differences under well controlled conditions.

631 In contrast to the inhibitory effect of ALA on bioreduction, ALA did not appear to
632 affect the chemical reduction rate and extent (Appendix 2). Three possible reasons
633 may be responsible for this difference between chemical and biological reduction.
634 First, because of the rapid rate of chemical reduction, the inhibitory/promoting factors
635 of ALA could not be manifested in such a short time span. Second, sodium dithionite
636 is a small molecule and can possibly enter the NAu-2 interlayer without any
637 impedance, even in the presence of ALA. Third, the fundamental difference in the
638 electron transfer mechanism between microbial and chemical reduction (Ribeiro et al.
639 2009; Stucki, 2011) may render ALA as an inefficient agent in blocking electron

transfer in the case of chemical reduction. All these reasons may have been responsible for the lack of any inhibitory/facilitation effect of ALA on chemical reduction.

New insights of the mechanisms of ALA release from NAu-2

Biological reduction and air re-oxidation. Biological reduction of structural Fe(III) in clay minerals is believed to proceed from the edge towards the interior of the structure (Ribeiro et al. 2009; Stucki, 2011) via a reduction front. With increasing extent of Fe(III) reduction, this reduction front progressivly moves from the exterior into the interior of NAu-2 particles. Because of a limited extent of bioreduction by various microorganisms (usually < 30%, Dong et al. 2009), it is likely that a large fraction of Fe(III) bioreduction is accomplished through clay edges (Fig. 12; Zhao et al. 2015). According to this model, only that fraction of intercalated ALA that was associated with clay edge may be released during the initial phase of Fe(III) reduction (Fig. 12, mechanism 1), likely due to its close proximity to aqueous solution and reduction-triggered structural instability. This ALA release mechanism would account for the splitting of the d(001) spacing from ~1.7 nm for unreduced ALA-NAu-2 into ~1.5-1.7 and ~1.2 nm for the bioreduced sample (Fig. 2) because ALA release would shrink the interlayer spacing of ALA-NAu-2 particles back to the original spacing of NAu-2. This model would also explain the heterogeneous distribtuion of carbon as a result of bioreduciton of ALA-NAu-2: e,g., depletion on the particle edges and enrichment in the interior (Fig. 10). This preferential release of ALA along NAu-2

edges also explains larger fringe spacings in the particle interior but smaller spacings around the edges (Fig. 11C). At the experimental pH (neutral), ALA should be deprotonated and its charge should be either neutral or negative, so its release from the nontronite interlayer is consistent with charge balance requirement.

Subsequent air re-oxidation would only convert the edge-Fe(II) back to Fe(III) with no further release of ALA, because this thin layer of Fe(II)-rich ALA-NAu-2 was already depleted in ALA (Fig. 12, mechanism 1). Our ALA release pattern (a small amount of ALA release at the beginning of bioreduction with no further release during subsequent oxidation, Fig. 6A) was consistent with this model. Reoxidation of Fe(II) to Fe(III) would create excess positive charge to the nontronite structure, and one mechanism to achieve charge balance is via removal of Na^+ from the interlayer. It is unlikely that ALA in aqueous solution would re-enter the interlayer in order to balance the charge because released ALA should have been either sorbed onto nontronite and bacterial cell surfaces or precipitated.

NAu-2 particle heterogeneity could be another reason for the observed ALA release. The broad XRD peaks for unreduced NAu-2 (Fig. 2A) suggest that this mineral was heterogeneous in particle size (surface area), thickness, and crystallinity (Yang et al. 2012). The intercalation of ALA into the interlayer of NAu-2 and adsorption of ALA onto NAu-2 particle surfaces could have introduced additional NAu-2 particle heterogeneities, as evidenced by the broadening of the (001) peak of ALA-NAu-2 (Fig. 2B) relative to NAu-2 (Fig. 2A). Based on our previous observation that small and poorly crystalline particles should be preferentially

684 subjected to reductive dissolution (Yang et al. 2012; Zhao et al., 2015), it is likely that
685 reductive dissolution of these particles released a small amount of ALA at the
686 beginning of the bioreduction experiments. This model would explain the
687 "purification effect" (e.g. peak sharpening" as revealed by XRD and FTIR (Table. 2;
688 Fig. 2; Fig. 3). That is, after reductive dissolution of the small and/or poorly
689 crystalline particles, the molecular interaction between ALA and NAu-2 in the
690 residual but more crystalline ALA-NAu-2 particles would be stronger, and would
691 result in sharper peaks in XRD patterns and more intense absorption bands in FTIR
692 spectra. These lines of evidence collectively suggest that the fraction of ALA
693 associated with small and/or poorly crystalline particles was unstable and
694 preferentially released during the iron redox cycle (Fig. 12, mechanism 2).

695 In summary, our results in this study demonstrated that ALA release pattern was
696 much more complex than the model proposed in our earlier study (Zhang et al., 2014).
697 The release of ALA throughout the iron redox cycle can be divided into three stages.
698 During the first stage (days 0-2) (Fig. 4B), the small and/or poorly crystalline particles
699 may be preferentially reduced and dissolved at the beginning of bioreduction, and a
700 small amount of the intercalated or adsorbed ALA was released from these particles.
701 During this stage, the amount of release ALA was positively correlated with the
702 bioreduction extent (Fig. 7), as consistent with the model proposed by Zhang et al.
703 (2014). During the second stage (days 2-32) (Fig. 4B), because a fraction of the
704 intercalated ALA had been already released from small/poorly crystalline particles,
705 continued bioreduction of structural Fe(III) in larger and well-crystalline NAu-2

706 particles would not release ALA any further (Fig. 6A). During the third stage (air
707 re-oxidation stage), although there was a small amount of dissolution (Table 1, Yang
708 et al. 2012), re-oxidation resulted in little ALA release because it occurred largely
709 around NAu-2 particle edges, which had already been stripped off ALA.
710
711 **Chemical reduction.** Because of the major differences in the mechanism between
712 chemical and biological reduction (Lee et al. 2006; Stucki, 2011; Stucki and Kostka,
713 2006), the pattern of ALA release was expected to be different. In contrast to the
714 reduction front model (Ribeiro et al. 2009;), chemical reduction follows a "pseudo
715 random" model, in which electron transfer from the reductant to structural Fe(III) in
716 the octahedral sites is virtually random and does not exhibit much selectivity (Ribeiro
717 et al. 2009), especially in Fe-rich clays like nontronite (Neumann et al. 2011). In this
718 case, ALA in any part of the NAu-2 structure (not necessarily limited to edge sites)
719 would be equally susceptible to reductive release. Because of rapid and extensive
720 dissolution (Table 1 and Fig. 9G, H), chemical reductant may have resulted in a
721 homogeneous release of ALA from all particles. In this case, a large fraction of ALA
722 would be expected to release from intercalated/adsorbed ALA (Table. 1).
723
724 **Mineral transformation**
725 In contrast to our early study (Zhang et al., 2014), where no mineralogical
726 changes were observed as a result of Fe(III) bioreduction by methanogens, our XRD,
727 SEM, and TEM all demonstrated extensive mineralogical changes as a result of Fe(III)

728 bioreduction by iron-reducing bacteria. The formation of albite and silica is consistent
729 with our earlier studies (Liu et al., 2015; Zhao et al., 2015) and supports our ALA
730 release model, e.g., reductive dissolution of small and poorly crystalline NAu-2
731 particles. Relative to the biogenic albite formed from microbial reduction of Fe(III) in
732 pure NAu-2 (Zhao et al., 2015), the size of the albite observed in this study was
733 several times larger, suggesting that ALA may have played an effect in its formation
734 and growth.

735

736 **Preservation of ALA in NAu-2 against iron redox cycling**

737 Oscillating redox conditions are common in natural environments such as the
738 wetting-drying cycle of rice paddy soils (Favre et al. 2006; Stucki, 2011). Under such
739 conditions, the extent and rate of organic matter decomposition would be determined
740 by their chemical recalcitrance (Baldock and Skjemstad, 2000; Lützow et al. 2006),
741 oxygen exposure time (Hartnett et al. 1998) and its physico-chemical protection from
742 decomposition (Conant et al. 2011). A previous study indicated that even a brief,
743 periodic exposure to O_2 would result in extensive and sometimes rapid organic matter
744 decomposition (Aller, 1994). Under long-term oxygen exposure, even organic
745 matter-mineral aggregates would be destroyed (Arnarson and Keil, 2007). Thus, an
746 oscillating redox condition clearly affects organic matter burial and preservation in
747 natural environment.

748 Our results demonstrated that after ALA removal from the edges of small/poorly
749 crystalline NAu-2 particles, ALA preserved in the nontronite structure was virtually

not released throughout the iron redox cycle (Fig. 6). After one complete redox cycle of iron, NAu-2 clay particles appeared aggregated (Fig. 9E) which would be resistant to further ALA loss. A reasonable prediction is that these aggregates may be able to better protect ALA from degradation even if they are subjected to more iron redox cycles. However, more research is needed to confirm this prediction. In comparison with complicated natural system, there are many limitations in laboratory experiments such as the short experimental time frame, the use of iron-rich clay mineral, and the simplicity of the experiments, but these results are valuable as they provide mechanistic insights into the role of clay minerals in preserving organic compound in redox oscillating environment.

IMPLICATION

Although the type of association between mineral and organic matter varies depending on the physical and chemical properties of the organic molecules and the minerals of interest (Keil and Mayer, 2014; Kleber et al. 2014), there is little doubt that sorption of organic matter onto mineral surfaces will protect it from degradation. While much evidence found in natural environment suggests that natural organic matter is either adsorbed onto mineral surfaces or occluded in the space formed by aggregation of irregular mineral particles (Keil and Mayer, 2014; Lützow et al. 2006), not enough evidence has been found for organic matter intercalation into the interlayers of clay minerals as a protection mechanism. This gap in knowledge may be due to lack of appropriate characterization methods to characterize the intercalated

772 organic matter quantitatively (Alexandre and Dubois, 2000). Our results demonstrated
773 that certain organic compound can be effectively protected within the interlayers of
774 clay mineral structures against a changing redox environment and this protection may
775 be responsible for the observed positive correlation between the total organic carbon
776 content and the mineral surface area of sediments and sedimentary rocks (including
777 both external and internal surface areas) (Kennedy et al. 2002; 2006). Relative to the
778 external mineral surfaces or the interstitial pore space with mineral aggregates, the
779 interlayer region of expandable clay minerals may be a better shelter because this
780 region may not be readily accessible to geochemical weathering agents and may resist
781 the negative effects induced by changing environments (such as redox condition). It is
782 also a potential site for hydrocarbon generation (Yuan et al. 2013). Thus, it is possible
783 that the amount of organic matter preserved in the interlayers of clay minerals,
784 especially expandable clay mineral such as smectite, may be higher than previously
785 known.

786 Our results further revealed that one way to release organic matter from the
787 interlayer region of clay minerals is via intense chemical reduction with strong
788 chemical reductant such as sodium dithionite. However, chemically active reductants
789 are not commonly present in natural environment. So this type of extreme condition
790 should be rare in nature. Nevertheless, our results do support the reliability of a
791 previously reported method of using chemical reduction to determine the amount of
792 organic carbon associated with reactive iron phases in sediments of varying
793 mineralogy (Lalonde et al. 2012).

Our results also have implications for the industry-scale purification process of organominerals. For commercial organoclays, the purity and surfactant loadings can significantly affect their thermal stability (Cui et al. 2008), and thus pose a serious concern. The removal of organic impurities using the traditional methods such as washing may be incomplete (Bellucci et al. 2006). Our data suggest that microbial reduction of structural iron in organoclays can release the poorly-sorbed organic impurity, especially those associated with small/poorly crystalline clay particles while at the same time preserving the organic matter in the interlayer of larger and well-crystalline clay particles. Chemical reduction could be an alternative option if more extensive leaching of organic matter is desired. Although still much research needs to be performed to assess the potential industrial application of our method, this study provides a possible alternative to purify industrial organoclays.

Acknowledgments

This work was supported by grants from the National Basic Research Program of China (No. 2012CB822004) and the Natural National Science Foundation of China (41030211). We thank Peng Yuan at the Institute of Geochemistry, Chinese Academy of Science for help in ALA-nontronite synthesis. We are grateful to two anonymous reviewers whose comments improved the quality of the manuscript.

References

Abken, H.J., Tietze, M., Brodersen, J., Bäumer, S., Beifuss, U., and Deppenmeier, U. (1998) Isolation and characterization of methnophenazine and function of phenazines in membrane-bound elevtron transport of Methanosarcina mazi Gö1. Journal of Bacteriology, 180, 2027–2032.

Alexandre, M., and Dubois, P. (2000) Polymer-layered silicate nanocomposites: preparation, properties and uses of a new class of materials. Materials Science and Engineering: R: Reports, 28, 1-63.

Aller, R.C. (1994) Bioturbation and remineralization of sedimentary organic matter: effects of redox oscillation. Chemical Geology, 114, 331-345.

Amonette, J.E., and Templeton, J.C. (1998) Improvements to the quantitative assay of nonrefractory minerals for Fe (II) and total Fe using 1, 10-phenanthroline. Clays and Clay Minerals, 46, 51-62.

Anderson, D., Saggar S., Bettany, J., and Stewart, J.(1981) Particle size fractions and their use in studies of soil organic matter: I. The nature and distribution of forms of carbon, nitrogen, and sulfur. Soil Science Society of America Journal, 45, 767-772.

Arnarson, T.S., and Keil, R.G. (2001) Organic–mineral interactions in marine sediments studied using density fractionation and X-ray photoelectron spectroscopy. Organic Geochemistry, 32, 1401-1415.

Arnarson, T.S., and Keil, R.G. (2007) Changes in organic matter–mineral interactions

for marine sediments with varying oxygen exposure times. Geochimica et Cosmochimica Acta, 71, 3545-3556.

Baldock, J.A., and Skjemstad, J. (2000) Role of the soil matrix and minerals in protecting natural organic materials against biological attack. Organic Geochemistry, 31, 697-710.

Bellucci, F., Camino, G., Frache, A., Ristori, V., Sorrentino, L., Iannace, S., Bian, X., Guardasole, M., and Vaccaro, S. (2006) Effect of organoclay impurities on mechanical properties of EVA-layered silicate nanocomposites. e-Polymers, **6**, 185-194.

Bergamaschi, B.A., Tsamakis, E., Keil, R.G., Eglinton, T.I., Montluçon, D.B., and Hedges, J.I. (1997) The effect of grain size and surface area on organic matter, lignin and carbohydrate concentration, and molecular compositions in Peru Margin sediments. Geochimica et Cosmochimica Acta, 61, 1247-1260.

Bishop, M.E., Dong, H., Kukkadapu, R.K., Liu, C., and Edelmann, R.E. (2011) Bioreduction of Fe-bearing clay minerals and their reactivity toward pertechnetate (Tc-99). Geochimica et Cosmochimica Acta, 75, 5229-5246.

Bock, M.J., and Mayer, L.M. (2000) Mesodensity organo–clay associations in a near-shore sediment. Marine Geology, 163, 65-75.

Choi, O., Deng, K.K., Kim, N.J., Ross, Jr. L., Surampalli, R.Y., and Hu, Z. (2008) The inhibitory effects of silver nanoparticles, silver ions, and silver chloride colloids on microbial growth. Water Research, 42, 3066-3074.

Conant, R.T., Ryan, M.G., Ågren, G.I., Birge, H.E., Davidson, E.A., Eliasson, P.E.,

858 Evans, S.E., Frey, S.D., Giardina, C.P., Hopkins, F.M., and others (2011)
859 Temperature and soil organic matter decomposition rates–synthesis of current
860 knowledge and a way forward. Global Change Biology, 17, 3392-3404.
861 Cui, L., Khramov, D.M., Bielawski, C.W., Hunter, D., Yoon, P., and Paul, D. (2008)
862 Effect of organoclay purity and degradation on nanocomposite performance, Part
863 1: Surfactant degradation. Polymer, 49, 3751-3761.
864 Dong, H., Kukkadapu, R.K., Fredrickson, J.K., Zachara, J.M., Kennedy, D.W. and
865 Kostandarithes, H.M. (2003) Microbial reduction of structural Fe(III) in illite and
866 goethite. Environmental Science & Technology, 37, 1268–1276.
867 Dong, H., Jaisi, D.P., Kim, J., and Zhang, G. (2009) Microbe-clay mineral interactions.
868 American Mineralogist, 94, 1505-1519.
869 Dong, H. (2012) Clay–microbe interactions and implications for environmental
870 mitigation. Elements, 8, 113-118.
871 Emerson, D., Fleming, E.J., and McBeth, J.M. (2010) Iron-oxidizing bacteria: an
872 environmental and genomic perspective. Annual Review of Microbiology, 64,
873 561-583.
874 Favre, F., Bogdal, C., Gavillet, S., and Stucki, J.W. (2006) Changes in the CEC of a
875 soil smectite–kaolinite clay fraction as induced by structural iron reduction and
876 iron coatings dissolution. Applied Clay Science, 34, 95-104.
877 Fredrickson, J.K., Zachara, J.M., Kennedy, D.W., Dong, H., Onstott, T.C., Hinman,
878 N.W., and Li, S.M. (1998). Biogenic iron mineralization accompanying the
879 dissimilatory reduction of hydrous ferric oxide by a groundwater bacterium.

880 Geochimica et Cosmochimica Acta, 62, 3239-3257.

881 Hedges, J.I., and Hare, P. (1987) Amino acid adsorption by clay minerals in distilled
882 water. Geochimica et Cosmochimica Acta, 51, 255-259.

883 Houghton, J.T. (1996) Climate change 1995: The science of climate change:
884 contribution of working group I to the second assessment report of the
885 Intergovernmental Panel on Climate Change (Vol. 2), p. 3-45. Cambridge
886 University Press, U.K.

887 Jaisi, D.P., Kukkadapu, R.K., Eberl, D.D., and Dong, H. (2005) Control of Fe(III) site
888 occupancy on the rate and extent of microbial reduction of Fe(III) in nontronite.
889 Geochimica et Cosmochimica Acta, 69, 5429–5440.

890 Jaisi, D.P., Dong, H., and Morton, J.P. (2008a) Partitioning of Fe (II) in reduced
891 nontronite (NAu-2) to reactive sites: Reactivity in terms of Tc (VII) reduction.
892 Clays and Clay Minerals, 56, 175-189.

893 Jaisi, D.P., Liu, C., Dong, H., Blake, R.E., and Fein, J.B. (2008b) Fe^{2+} sorption onto
894 nontronite (NAu-2). Geochimica et Cosmochimica Acta, 72, 5361-5371.

895 Johnson, K.S., Gordon, R.M., and Coale, K.H. (1997) What controls dissolved iron
896 concentrations in the world ocean? Marine Chemistry, 57, 137-161.

897 Jones, D. and Edwards, A. (1998) Influence of sorption on the biological utilization of
898 two simple carbon substrates. Soil Biology and Biochemistry, 30, 1895-1902.

899 Kaiser, K., and Guggenberger G. (2000) The role of DOM sorption to mineral surfaces
900 in the preservation of organic matter in soils. Organic Geochemistry, 31, 711-725.

901 Katti, K.S., Katti, D.R., and Dash, R. (2008) Synthesis and characterization of a novel

chitosan/montmorillonite/hydroxyapatite nanocomposite for bone tissue engineering. Biomedical Material, 3, 034122.

Katti, K.S., Sikdar, D., Katti, D.R., Ghosh, P., and Verma, D. (2006) Molecular interactions in intercalated organically modified clay and clay–polycaprolactam nanocomposites: experiments and modeling. Polymer, 47, 403-414.

Keeling, J.L., Raven, M.D., and Gates, W.P. (2000) Geology and characterization of two hydrothermal nontronites from weathered metamorphic rocks at the Uley graphite mine, South Australia. Clays and Clay Minerals, 48, 537-548.

Keil, R.G., and Mayer, L.M. (2014) Mineral Matrices and Organic Matter, In Turekian, H.D. and Holland K.K. Ed., Treatise on Geochemistry (Second Edition), p. 337-359. Elsevier Press, Oxford.

Keil, R.G., Montluçon, D.B., Prahl, F.G., and Hedges, J.I. (1994a) Sorptive preservation of labile organic matter in marine sediments. Nature, 370, 549-552.

Keil, R.G., Tsamakis, E., Fuh, C.B., Giddings, J.C., and Hedges, J.I. (1994b) Mineralogical and textural controls on the organic composition of coastal marine sediments: Hydrodynamic separation using SPLITT-fractionation. Geochimica et Cosmochimica Acta, 58, 879-893.

Kennedy, M., Droser, M., Mayer, L.M., Pevear, D., and Mrofka, D. (2006) Late Precambrian oxygenation; inception of the clay mineral factory. Science, 311, 1446-1449.

Kennedy, M.J., Pevear, D.R., and Hill, R.J. (2002) Mineral surface control of organic carbon in black shale. Science, 295, 657-660.

924 Kleber, M., Eusterhues, K., Keiluweit, M., Mikutta, C., Mikutta, R., Nico, P.S. (2014).
925 Mineral–Organic Associations: Formation, Properties, and Relevance in Soil
926 Environments. Advances in Agronomy, 30, 1-140.
927 Lützow, M.V, Kögel-Knabner, I., Ekschmitt, K., Matzner, E., Guggenberger, G.,
928 Marschner, B., Flessa, H. (2006) Stabilization of organic matter in temperate soils:
929 mechanisms and their relevance under different soil conditions–a review.
930 European Journal of Soil Science, 57, 426-445.
931 Lalonde, K., Mucci, A., Ouellet, A., and Gélinas Y. (2012) Preservation of organic
932 matter in sediments promoted by iron. Nature, 483, 198-200.
933 Lee, K., Kostka, J.E., and Stucki, J.W. (2006) Comparisons of structural Fe reduction
934 in smectites by bacteria and dithionite: An infrared spectroscopic study. Clays and
935 Clay Minerals, 54, 195-208.
936 Liu, D., Dong, H., Wang, H., and Zhao, L. (2015) Low-temperature feldspar and illite
937 formation through bioreduction of Fe(III)-bearing smectite by an alkaliphilic
938 bacterium. Chemical Geology, 406, 25-33.
939 Liu, M.T., Pu, M.F., Ma, H.W., Hu, Y.F., Liu, X., J. and Pang, X. (2011) The effect of
940 organic modifier-12-aminolauric acid on morphology and thermal properties of
941 polylactide nanocomposites. Polymer Composites, 32, 1002-1008.
942 Lovley, D.R., Holmes, D.E., and Nevin, K.P. (2004) Dissimilatory Fe (III) and Mn
943 (IV) reduction. Advances in Mcrobial Physiology,49, 219-286.
944 Mayer, L.M. (1999) Extent of coverage of mineral surfaces by organic matter in
945 marine sediments. Geochimica et Cosmochimica Acta**,** 63, 207-215.

946 Mayer, L.M. (1994a) Relationships between mineral surfaces and organic carbon
947 concentrations in soils and sediments. Chemical Geology, 114, 347-363.
948 Mayer, L.M. (1994b) Surface area control of organic carbon accumulation in
949 continental shelf sediments. Geochimica et Cosmochimica Acta, 58, 1271-1284.
950 McGill, W., and Cole, C. (1981) Comparative aspects of cycling of organic C, N, S
951 and P through soil organic matter. Geoderma, 26, 267-286.
952 Melton, E.D., Swanner, E.D., Behrens, S., Schmidt, C., and Kappler, A. (2014) The
953 interplay of microbially mediated and abiotic reactions in the biogeochemical Fe
954 cycle. Nature Reviews Micorbiology, 12, 797-808.
955 Newman, D.K. and Kolter, R. (2000) A role for excreted quinones in extracellular
956 electron transfer. Nature, 405, 94-97.
957 Neumann, A., Olson, T.L., and Scherer, M.M. (2013) Spectroscopic Evidence for Fe
958 (II)–Fe (III) Electron Transfer at Clay Mineral Edge and Basal Sites.
959 Environmental Science & Technology, 47, 6969-6977.
960 Neumann, A., Petit, S., and Hofstetter, T.B. (2011) Evaluation of redox-active iron
961 sites in smectites using middle and near infrared spectroscopy. Geochimica et
962 Cosmochimica Acta, 75, 2336-2355.
963 Pentráková, L., Su, K., Pentrák, M., and Stucki, J. (2013) A review of microbial redox
964 interactions with structural Fe in clay minerals. Clay Minerals, 48, 543-560.
965 Ransom, B., Kim, D., Kastner, M., and Wainwright, S. (1998) Organic matter
966 preservation on continental slopes: importance of mineralogy and surface area.
967 Geochimica et Cosmochimica Acta, 62, 1329-1345.

Ribeiro, F.R., Fabris, J.D., Kostka, J.E., Komadel, P., and Stucki J.W. (2009) Comparisons of structural iron reduction in smectites by bacteria and dithionite: II. A variable-temperature Mössbauer spectroscopic study of Garfield nontronite. Pure & Applied Chemistry, 81,1499-1509.

Sikdar, D., Katti, D.R., and Katti, K.S. (2006a) A molecular model for ε-caprolactam-based intercalated polymer clay nanocomposite: integrating modeling and experiments. Langmuir, 22, 7738-7747.

Sikdar, D., Katti, D.R., Katti, K.S., and Bhowmik, R. (2006b) Insight into molecular interactions between constituents in polymer clay nanocomposites. Polymer, 47, 5196-5205.

Sikdar, D., Katti, K.S., and Katti, D.R. (2008) Molecular interactions alter clay and polymer structure in polymer clay nanocomposites. Journal of Nanoscience & Nanotechnology, 8, 1638-1657.

Stucki, J.W., Bailey, G.W., and Gan, H. (1996) Oxidation-reduction mechanisms in iron-bearing phyllosilicates. Applied Clay Science, 10, 417-430.

Stucki, J.W., and Kostka, J.E. (2006) Microbial reduction of iron in smectite. Comptes Rendus Geoscience, 338, 468-475.

Stucki, J.W. (2011) A review of the effects of iron redox cycles on smectite properties. Comptes Rendus Geoscience, 343, 199-209.

Theng, B.K.G., and Newman, R. (1986) The occurrence of interlayer clay-organic complexes in two New Zealand soils. Soil Science, 142, 262-266.

Wattel-Koekkoek, E.J.W., Van Genuchten, P.P.L., Buurman, P., and Van Lagen, B.

(2001). Amount and composition of clay-associated soil organic matter in a range of kaolinitic and smectitic soils. Geoderma, 99, 27-49.

Weber, K.A., Achenbach, L.A., and Coates, J.D. (2006) Microorganisms pumping iron: anaerobic microbial iron oxidation and reduction. Nature Reviews Microbiology, 4, 752-764.

Yang, J., Kukkadapu, R.K., Dong, H. Shelobolina, E.S., Zhang, J., and Kim, J. (2012) Effects of redox cycling of iron in nontronite on reduction of technetium. Chemical Geology, 291, 206-216.

Yuan, P., Liu, H., Liu, D., Tan, D., Yan, W., & He, H. (2013). Role of the interlayer space of montmorillonite in hydrocarbon generation: An experimental study based on high temperature–pressure pyrolysis. Applied Clay Science, 75, 82-91.

Zhang, G., Kim, J., Dong, H., and Sommer, A.J. (2007) Microbial effects in promoting the smectite to illite reaction: Role of organic matter intercalated in the interlayer. American Mineralogist, 92, 1401-1410.

Zhang, J., Dong, H., Liu, D., and Agrawal, A. (2013) Microbial reduction of Fe (III) in smectite minerals by thermophilic methanogen Methanothermobacter thermautotrophicus. Geochimica et Cosmochimica Acta, 106, 203-215.

Zhang, J., Dong, H., Zeng, Q., and Agrawal, A. (2014) The role of Fe(III) bioreduction by methanogens in the preservation of organic matter in smectite. Chemical Geology, 389, 16-28.

Zhao, L., Dong, H., Kukkadapu, R.K., Zeng, Q., Edelmann, R., Pentrák, M., and Agrawal, A. (2015). Biological Redox Cycling of Iron in Nontronite and its

Potential Application in Nitrate Removal. Environmental science & technology, 49, 5493-5501.

FIGURE CAPTION

Fig. 1. Pictures showing different dispersion behaviors between NAu-2 (left) ALA-NAu-2 (right). B, C, D and E are SEM images and corresponding EDS analyses for NAu-2 and ALA-NAu-2.

Fig. 2. XRD patterns of air-dried samples showing the changes of the d(001) spacing after different treatments of ALA-NAu-2 in comparison with NAu-2. A). Abiotic NAu-2 control; B). Abiotic ALA-NAu-2 control; C). Bioreduced ALA-NAu-2 (without AQDS); D). Bioreduced ALA-NAu-2 (with AQDS); E). Bioreduced, air re-oxidized ALA-NAu-2 (the same pattern regardless of AQDS); h). Chemically reduced ALA-NAu-2 (28.6% reduction extent); i). Chemically reduced NAu-2 (reduction extent 81.2%).

Fig. 3. Fourier-transform infrared spectra for NAu-2 and ALA-NAu-2 that were either biologically or chemically reduced followed by air re-oxidation over different regions of wave number. a). Unaltered NAu-2; b). ALA; c). Mechanical mixture of NAu-2 and ALA; d) Unreduced ALA-NAu-2; d). e). Bioreduced ALA-NAu-2; f). Bioreduced NAu-2; g). Bioreduced, air re-oxidized ALA-NAu-2; h). Chemically reduced ALA-NAu-2 (reduction extent 25%); i). Chemically reduced NAu-2 (reduction extent

1034 25%).

1035

1036 Fig. 4.Time-course production of total Fe(II) in NAu-2 and ALA-NAu-2 as measured
1037 by the 1,10-phenanthroline method. Initial cell concentration was 10^8 cells/mL.
1038 Averages of two measurements from duplicate experimental tubes are reported. The
1039 error bars represent the higher and lower values. Control did not have any cells.

1040

1041 Fig. 5. Time-course re-oxidation of Fe(II) in ALA-NAu-2 and NAu-2 as measured by
1042 the 1,10-phenanthroline method. The inset is an enlargement of the graph over the
1043 0–12 hour period.

1044

1045 Fig. 6. Time-course decrease of TOC content (wt %) in NAu-2 and ALA-NAu-2 over
1046 the course of Fe(III) reduction and air re-oxidation of Fe(II) (A). Bioreduction
1047 followed by air re-oxidation; (B). Chemical reduction followed by air re-oxidation.
1048 For NAu-2, there is no difference in TOC release pattern between abiotic control and
1049 bioreduced samples (open cycles in Fig. 6A).

1050

1051 Fig. 7. Correlation between ferrous iron content and TOC during bioreduction and air
1052 re-oxidation process.

1053

1054 Fig. 8. Deconvolution of the (001) peak for the bioreduced ALA-NAu-2 with AQDS.
1055 Fit peak 1 represents the peak at d = 16.6 Å; Fit peak 2 represents the peak with d =

12.8Å. The grey areas represent the relative weight percentages of the ALA-NAu-2 and NAu-2.

Fig. 9. Secondary electron images showing NAu-2 and ALA-NAu-2 particles after bioreduction, air re-oxidation, and chemical reduction. A) Lamella-like (a1) and platy (a2) particles in bioreduced ALA-NAu-2; B) Net-like particle morphology with many dissolution pits in bioreduced NAu-2; C) Albite in bioreduced ALA-NAu-2; D) Silica aggregates in bioreduced ALA-NAu-2; E) Particle aggregates in air re-oxidized ALA-NAu-2; F) Newly formed particles with a high carbon content in air re-oxidized ALA-NAu-2; G) Particles with rose and net-like morphologies in chemically reduced ALA-NAu-2 (28.6% reduction extent); H) Net-shaped ALA-NAu-2 particles in chemically reduced ALA-NAu-2 (81.2% reduction extent). The panels at the right side of the images show the corresponding EDS composition of those labeled particles (e.g. a1, a2, etc). The Pt peak came from sample coating.

Fig. 10. Elemental mapping of carbon in unreduced (A) and bioreduced (B) ALA-NAu-2 particles. A comparison between these two maps illustrate a carbon redistribution after bioreduction. Depletion occurs along edges and grain boundaries, whereas enrichment occurs locally.

Fig. 11. Lattice fringe images for bioreduced NAu-2 and ALA-NAu-2.A). Unreduced NAu-2 showing 1.2 nm layer spacing with a corresponding EDS spectrum; B)

1078 UnreducedALA-NAu-2 showing 1.5 nm layer spacing with a corresponding EDS
1079 spectrum; C). Bioreduced ALA-NAu-2 particles with a d(001) spacing of 1.5 nm; D)
1080 Bioreduced ALA-NAu-2 particles with a d(001) spacing of 1.1-1.2 nm.
1081
1082 Fig. 12. Schematics showing electron transfer pathway in ALA-NAu-2 and two
1083 proposed different ALA release mechanisms.
1084
1085
1086
1087
1088
1089
1090
1091
1092
1093
1094
1095
1096 Table 1. Aqueous concentrations of Al, Si, and Si in bioreduced, re-oxidized and
1097 chemically reduced NAu-2 and ALA-NAu-2
1098

		Aqueous Al (10^{-3}mmol/g)	Aqueous Fe (10^{-2}mmol/g)	Aqueous Si (10^{-1}mmol/g)	Reduction extent (%)
Bioreduction	Control	1.4±0.1	1.4±0.1	1.2±0.1	0
	NAu-2	1.0±0.3	3.9±0.3	3.0±0.1	25.0
	ALA-NAu-2	1.3±0.1	3.8±0.1	1.9±0.0	26.0
Abiotic air re-oxidation	Control	1.3±0.1	1.5±0.2	1.3±0.2	0
	NAu-2	6.6±0.1	10.9±0.2	4.6±0.0	2.4
	ALA-NAu-2	3.9±0.1	4.9±0.3	5.0±0.1	4.7
Chemical reduction of ALA-NAu-2 (diff. extent)	Control	1.2±0.2	1.6±0.1	1.4±0.2	0
	Experiment	81.6±1.3	69.3±1.2	14.5±0.2	28.5
		147.3±50.6	145.1±15.2	29.0±2.0	37.6
		242.4±11.2	205.6±10.3	39.9±1.9	50.0
		297.9±6.9	268.6±35.9	53.6±7.4	58.5
		314.3±12.7	260.1±8.5	52.2±2.3	68.3
		325.2±35.9	268.2±26.8	54.1±6.3	79.0

Table 2. Peak areas of some characteristic bands of ALA in bioreduced, re-oxidized, and chemically reduced ALA-NAu-2

Peak / Sample	NH_2 stretching at 3287 cm^{-1}	CH_2-CH_2 Asymmetric strecching at 2932 cm^{-1}	CH_2-CH_2 symmetric stretching at 2855 cm^{-1}	C=O stretching at 1711 cm^{-1}	N-H bending at 1627 cm^{-1}	CO-H bending At 1470 cm^{-1}
ALA-NAu-2	nd	1.2	3.84	0.53	2.10	0.36
Bioreduced ALA-NAu-2	4.35	2.96	8.01	1.35	4.44	0.70
Re-oxidized ALA-NAu-2	10.18	3.31	8.9	2.95	4.51	0.94
Chemically reduced ALA-NAu-2	nd	0.81	2.25	nd	0.84	0.07

nd: not detected.

Fig. 1

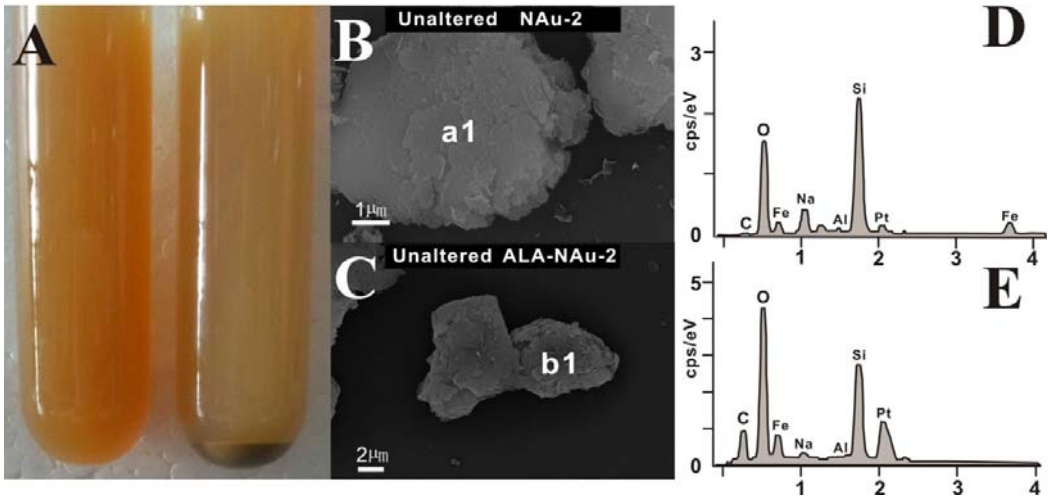

Fig. 1.

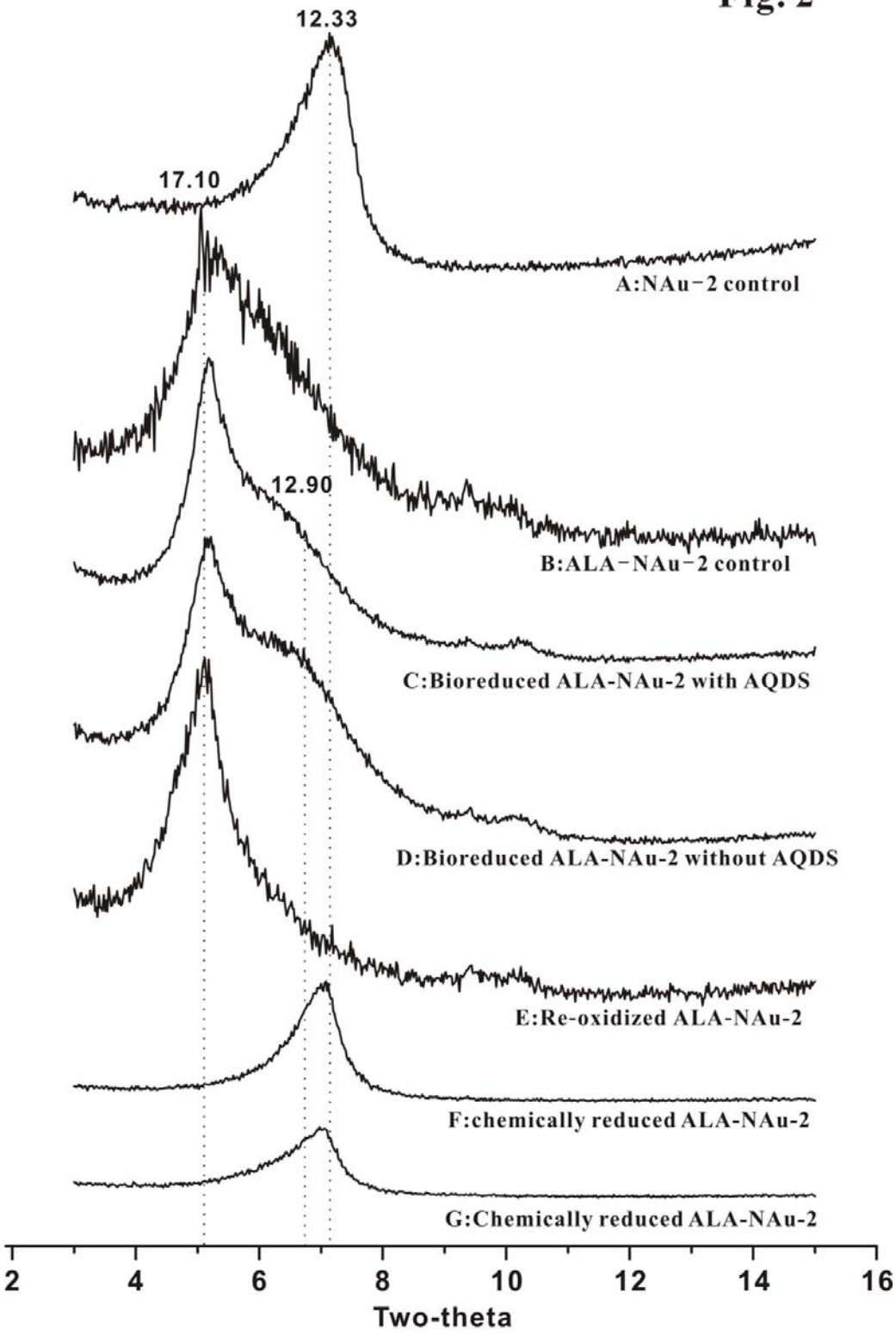

Fig. 2

Fig. 3

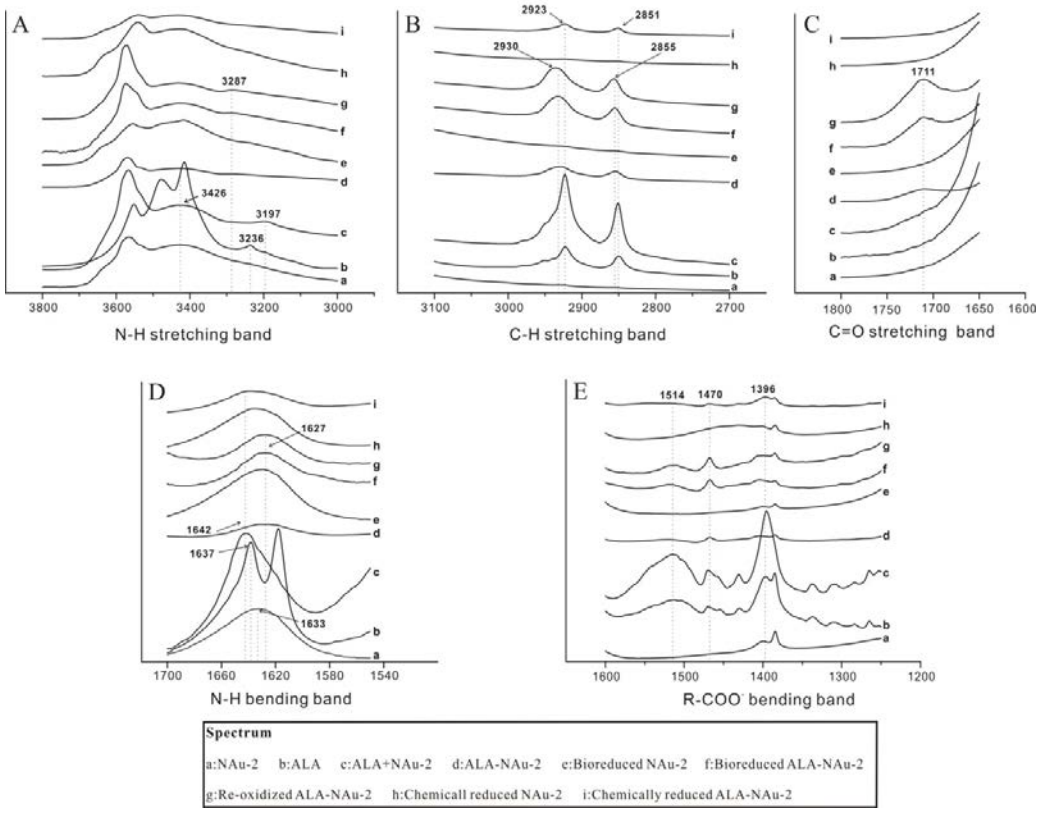

1113

1114 Fig. 3

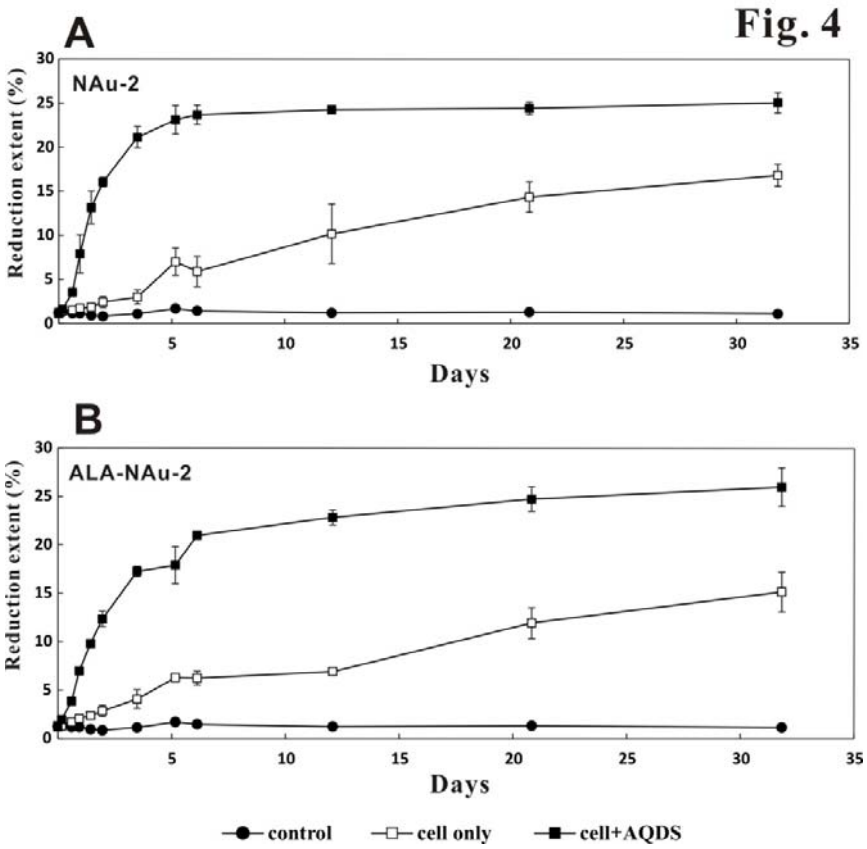

Fig. 4

Fig.5

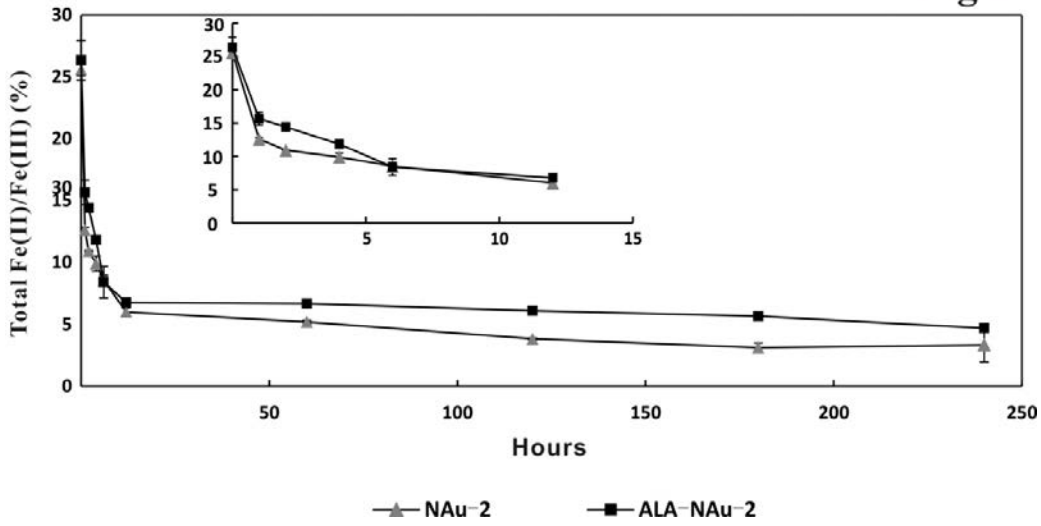

Fig. 5

Fig. 6

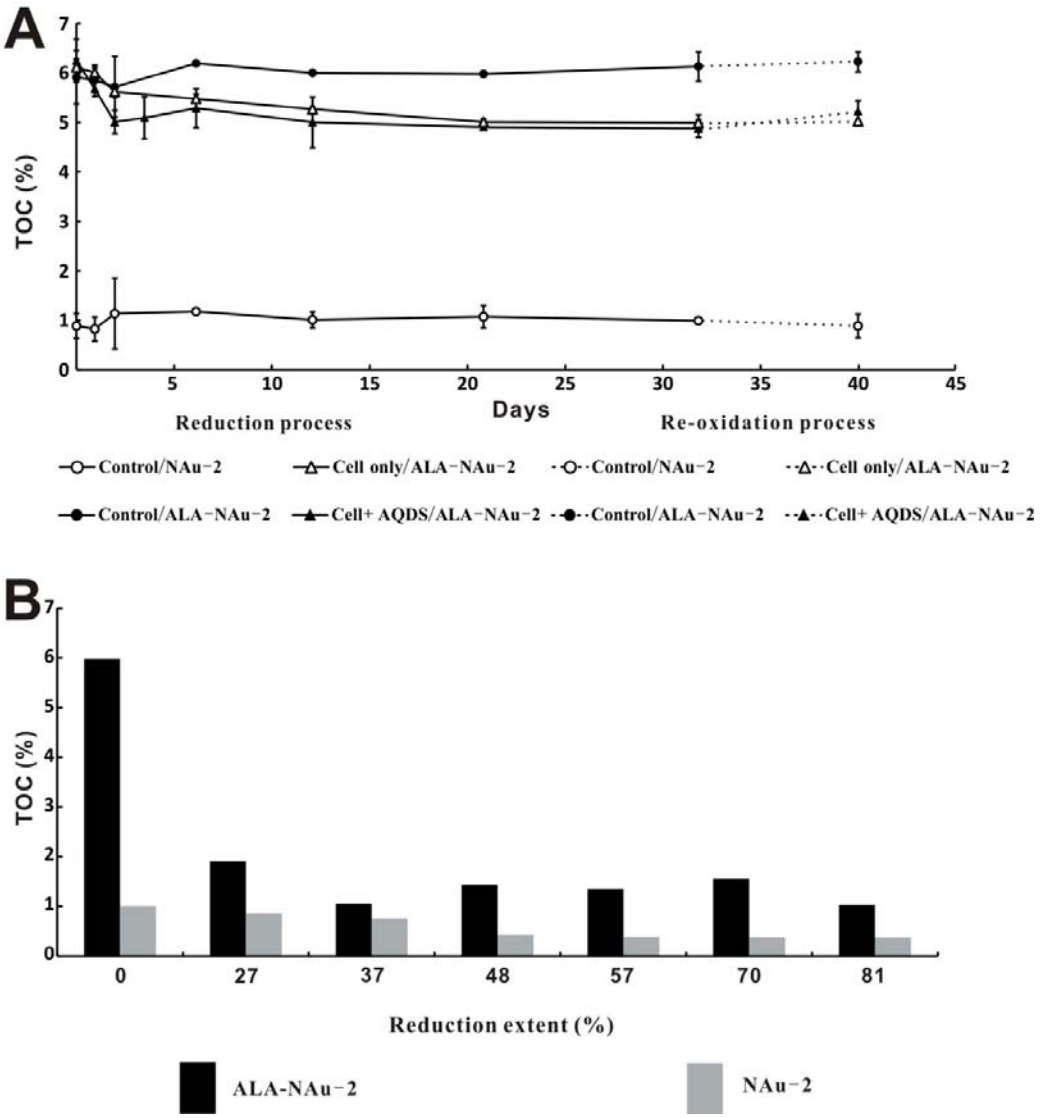

Fig. 6

Fig. 7

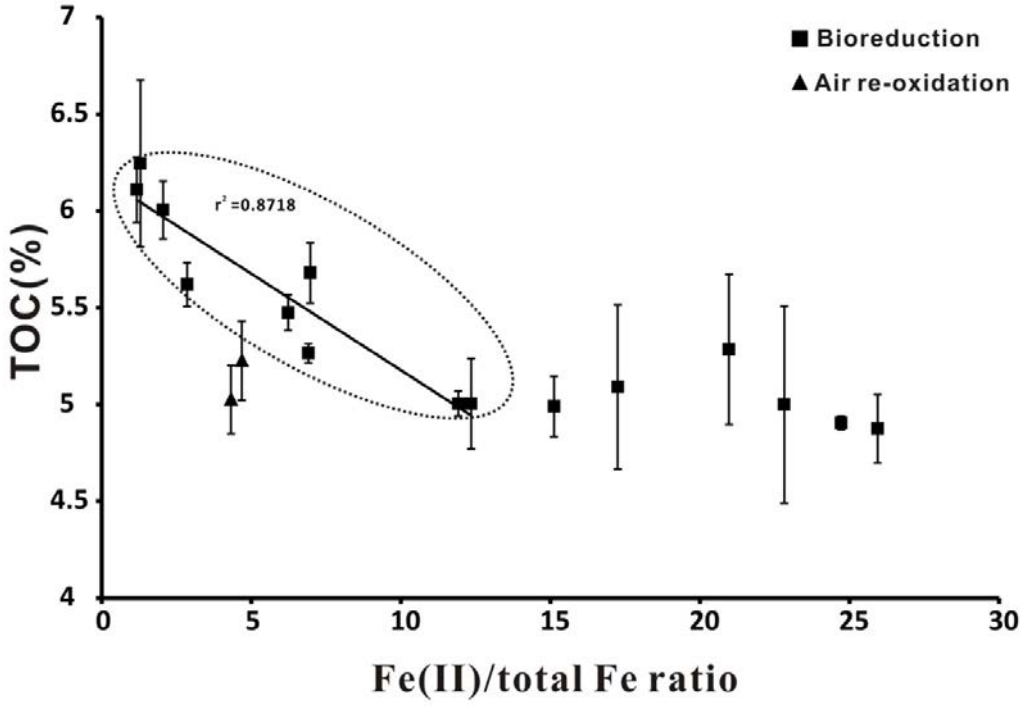

Fig. 7

Fig. 8

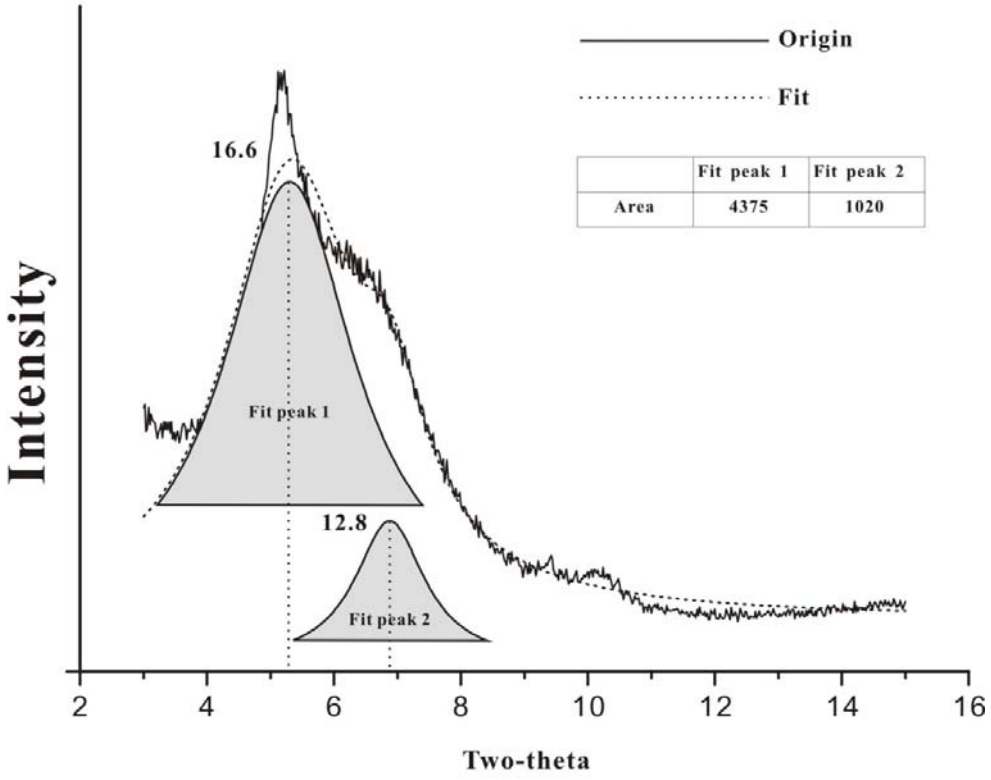

	Fit peak 1	Fit peak 2
Area	4375	1020

1129

1130 Fig. 8

Fig. 9

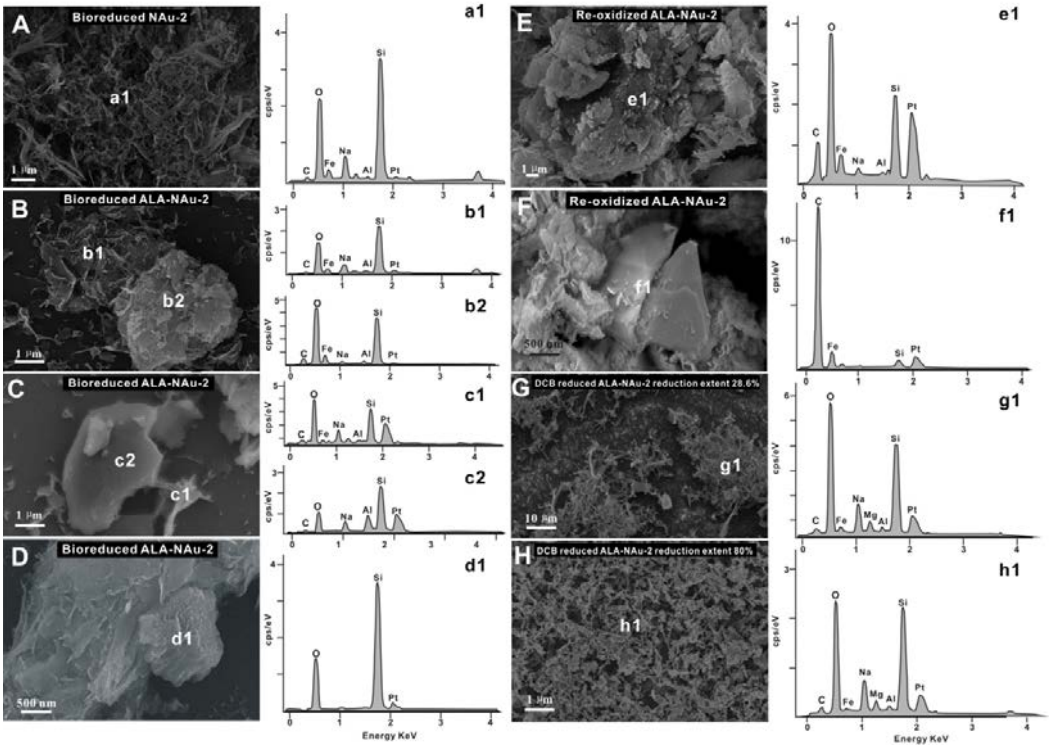

Fig. 9

Fig. 10

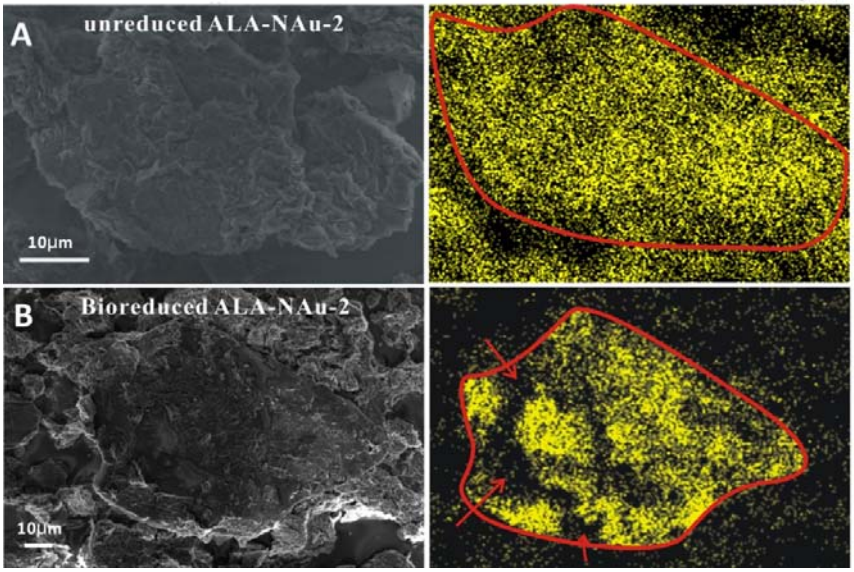

Fig. 10

Fig. 11

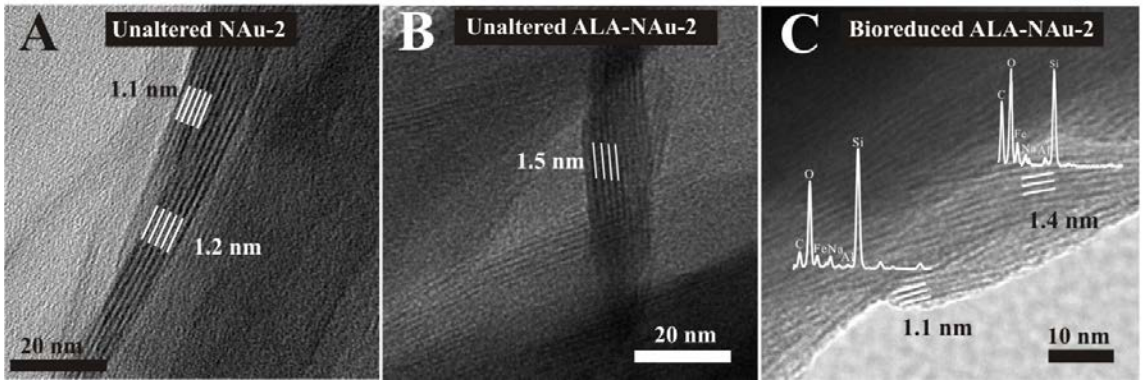

Fig. 11

1151

Fig. 12

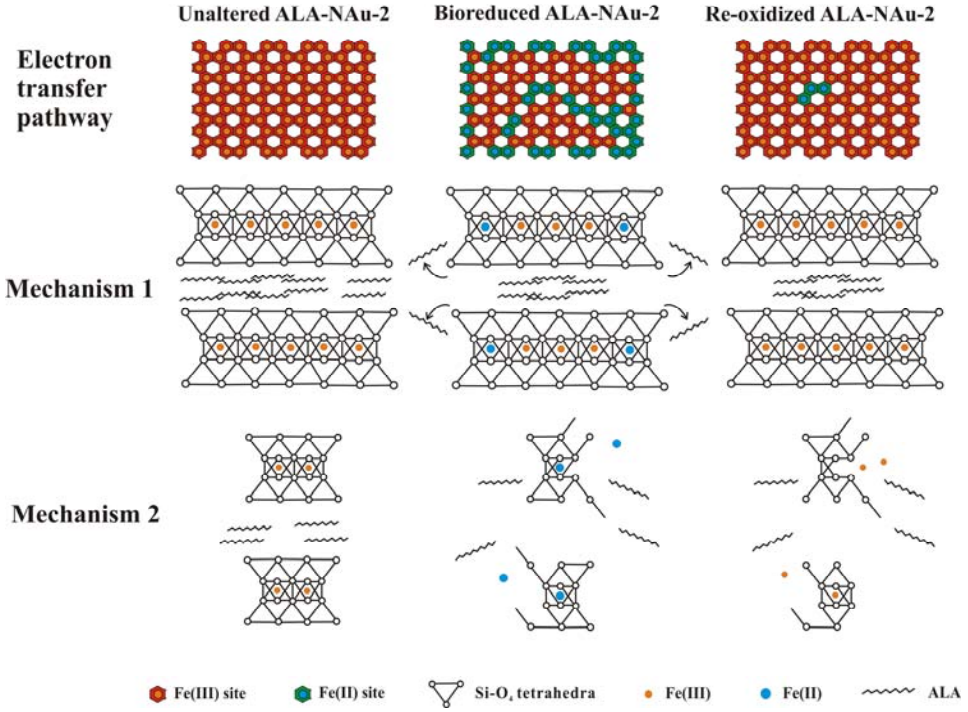

1152

1153

1154 Fig. 12